Robotica (2026), 1–25
doi:10.1017/S0263574726104019

RESEARCH ARTICLE

Extended state observer-sliding mode admittance control for grasping by the omnidirectional dexterous hand

Changlong Ye[1], Sixu Lu[1], Suyang Yu[2] and Huaiyong Li[2]

[1]School of Artificial Intelligence, Shenyang Aerospace University, China
[2]School of Mechatronics Engineering, Shenyang Aerospace University, China
Corresponding author: Suyang Yu; Email: yu_suyang@163.com

Received: 17 March 2026 UTC; **Revised:** 21 August 2026 UTC; **Accepted:** 30 August 2026 UTC

Keywords: control of robotic systems; force control; biomimetic robots; mechatronic systems; nonprehensile manipulation

Abstract

Compliant control of dexterous hands is increasingly demanded for environmental interaction. Conventional strategies often suffer from significant force tracking errors and poor adaptability when interacting with unknown environments. To meet the constant-force contact requirements in omnidirectional dexterous hand (ODH) grasping and object pose adjustment, this paper proposes an admittance control strategy integrating an extended state observer (ESO) with sliding mode control (SMC), termed extended state observer and sliding-mode admittance control. This method maintains the required contact forces for grasping and manipulation while demonstrating good adaptability to unknown object properties. A modified D-H method is employed to establish the kinematic model of the ODH, based on which its workspace and graspable object range are analyzed. Within the virtual mass-damping admittance framework, SMC is introduced to enhance the system's robustness against unknown environmental parameters. The ESO is utilized to estimate and compensate for the disturbance in the derivative of the force error, thereby reconstructing a smooth sliding surface to suppress chattering. Furthermore, a continuous SMC law is designed based on Lyapunov stability theory, guaranteeing stable convergence and smooth force tracking. Experimental results confirm that the proposed strategy can well track the desired grasping force and satisfy the requirements of grasping tasks. This work demonstrates the effectiveness of the proposed strategy in achieving robust and precise force control, offering a viable solution for the compliant manipulation of dexterous hands in complex environments.

1. Introduction

Advances in industrial automation [1–3], medical assistance [4, 5], and special-service robotics [6, 7] demand that dexterous hands, as end-effectors, possess high grasping capability, adaptability, and control precision. These have become critical metrics for overall system performance. In traditional robotic operation modes, the end-effector typically functions merely as a tool, with all compliant control relying solely on the manipulator body. When confronted with tasks that require sustained and stable contact force output, adaptation to dynamic interaction processes, unknown object parameters, or dexterous manipulation for object pose adjustment, these systems often exhibit limitations such as constrained force-tracking accuracy and weak environmental adaptability. This is primarily due to a mismatch in the manipulator's dynamic model, a lack of environmental perception, and insufficient fingertip dexterity.

To address issues such as constrained accuracy during robotic tasks due to unknown environmental parameters, numerous researchers worldwide have conducted extensive studies on compliant control strategies. Chen [8] proposed a variable admittance control (AC) method, which integrates the minimum-jerk model from motor science to extract velocity-curvature features for estimating indirect human intent and designing a guidance strategy. To achieve effective dynamic force tracking under time-varying end-effector trajectories, Pi [9] introduced an adaptive AC method that incorporates the

© The Author(s), 2026. Published by Cambridge University Press.

Downloaded from https://www.cambridge.org/core. UNIVERSIDAD AUTONOMA METROPOLITANA, on 19 Nov 2026 at 03:47:06, subject to the Cambridge Core terms of use, available at https://www.cambridge.org/core/terms. https://doi.org/10.1017/S0263574726104019

dynamic interaction states between the end-effector and the environment. For applications demanding precise contact force in unknown environments, Liu [10] proposed a smooth adaptive admittance controller. This controller generates a reference trajectory online and uses a feedforward PD loop to enhance robustness. Gao [11], addressing human–robot compatibility and collaborative control for lower-limb rehabilitation robots, first quantified and modeled human–robot interaction parameters and then designed an adaptive admittance dual-loop controller with RMSprop gain adjustment. Ye [12] presented a hybrid impedance-AC scheme for second-order unknown environments. Their method uses virtual inertia-impedance adaptation to derive an optimal target impedance model. Li [13] proposed an admittance controller that exploits the differentiability of collision contact force; it is formalized as a differential algebraic inclusion (DAI) with two interdependent set-valued loops. Jung [14] regulated the contact force indirectly in unknown environments by first modulating the impedance force through an admittance filter and then employing a position correction term. When confronting system modeling uncertainties and external unknown disturbances, other scholars have undertaken in-depth exploration to enhance the adaptability and robustness of AC. Researchers have integrated stability observers [15, 16] for real-time disturbance compensation, fuzzy inference systems [17, 18] for adaptive rule construction, and neural networks [19, 20] for learning-based adaptation. To varying degrees, these approaches improve the admittance controller's tolerance to parameter uncertainties, unmodeled dynamics, and environmental variations, thereby enhancing force-tracking accuracy and stability in complex interactions.

Despite these advances, existing admittance-based compliant control strategies share a fundamental limitation: their force-tracking performance depends heavily on the accuracy of the environmental stiffness model. When grasping objects made of unknown or varying materials, the actual stiffness often deviates from the nominal value assumed in the controller design. Under such conditions, several methods estimate the environmental stiffness or position online and adapt the controller accordingly [10, 21]. However, these approaches introduce additional complexity and remain sensitive to estimation accuracy; when the material properties are imprecisely known or change abruptly, the controller must be retuned, limiting its practicality in unstructured grasping tasks.

An alternative philosophy is to make the admittance dynamics inherently robust to parameter uncertainties, thereby eliminating the need for explicit stiffness identification or controller re-tuning. Sliding mode control (SMC) [22–24] offers precisely this capability—it can force the system state to remain on a prescribed sliding surface regardless of bounded parameter variations. Meanwhile, an extended state observer (ESO) can estimate and compensate for unmodeled dynamics and measurement noise in real time. However, the integration of SMC and ESO within the AC framework, specifically for force tracking in unknown environments, has not been systematically investigated.

To clarify the positioning of our work, Table I categorizes representative compliant control strategies, summarizes their key characteristics, and identifies the robot platform on which each method is implemented. This comparison reveals two gaps in the existing literature. First, from an architectural perspective, the vast majority of admittance-based controllers are deployed on robotic manipulators or collaborative robots, where the end-effector functions as a passive follower of the manipulator's motion. In contrast, we directly integrate AC into the dexterous end-effector, enabling the fingertips to actively regulate contact forces independently of the manipulator. Second, from a methodological perspective, most existing methods require either environmental parameter estimation or some form of prior knowledge. As a result, their force-tracking performance degrades when the object material is unknown or varies, limiting their practicality in grasping tasks.

To overcome these limitations, this paper proposes an ESO-based sliding mode admittance control (ESOSMCAC) strategy for the ODH grasping objects with unknown stiffness. The proposed method differs fundamentally from prior ESO-based admittance controllers in two respects. First, unlike approaches that use an ESO to estimate environmental parameters for controller adaptation, our ESO is tasked with estimating the noise in the force error derivative. This enables the reconstruction of a smooth sliding surface, effectively suppressing the chattering that would otherwise arise from direct numerical differentiation of noisy force signals. Second, rather than placing SMC in the inner position or force

Downloaded from https://www.cambridge.org/core. UNIVERSIDAD AUTONOMA METROPOLITANA, on 19 Nov 2026 at 03:47:06, subject to the Cambridge Core terms of use, available at https://www.cambridge.org/core/terms. https://doi.org/10.1017/S0263574726104019

Table I. *Comparison of representative compliant control strategies in terms of control method, robot platform, and key characteristics.*

Representative references	Method	Robot platform	Key characteristics
Pi et al. [9], Liu et al. [10], Gaoet al. [11]	Adaptive admittance control	Pure simulation/Robotic manipulator/ Lower limb rehabilitation robot	Online adjustment of admittance parameters or reference trajectory generation; typically requires environmental parameter estimation
Ye et al. [12]	Hybrid impedance–admittance control	2-DOF manipulator and 7-DOF Franka EMIKA panda robot	Combines both frameworks; still relies on virtual impedance model
Li et al. [13]	DAI-based admittance control	A dedicated Experimental Set-Up	Addresses non-differentiability of collision contact force; does not involve stiffness variation
Dao et al. [16]	Observer-based methods	Pure simulation	Observer estimates and compensates for disturbances; improves robustness against uncertainties
Toan et al. [17], Liu et al. [18], Almaghout et al. [19], Wang et al. [20]	Fuzzy/NN-based admittance control	Robotic manipulator/Lower-limb exoskeleton/ Knee rehabilitation robot/ Fracture reduction robot	Intelligent methods for adaptive rule construction; requires training data or expert rules
Zhu et al. [23]	Vision-admittance-based SMC	Collaborative robot (6-DOF)	Introduces SMC into admittance framework; some schemes rely on expert knowledge

control loop, we embed the sliding mode control (SMC) term directly into the virtual admittance model. This structurally modifies the admittance dynamics such that the force-tracking performance becomes insensitive to variations in object stiffness, obviating the need for stiffness identification or per-object parameter tuning. A continuous SMC law, designed via Lyapunov stability theory, guarantees stable convergence and smooth force tracking.

This paper is organized as follows: Section 2 describes the ODH mechanical structure, establishes its kinematic model, and analyzes its workspace as well as the range of graspable objects; Section 3 presents the ESOSMCAC strategy and provides theoretical stability analysis; Section 4 reports simulation and experimental results; and Section 5 concludes the study.

2. System model

2.1. Structure of the ODH

The ODH, as illustrated in Figure 1, comprises a deformation mechanism, a parallelogram mechanism, and four finger mechanisms. The deformation structure comprises an upper slider, a lower slider, and a

Downloaded from https://www.cambridge.org/core. UNIVERSIDAD AUTONOMA METROPOLITANA, on 19 Nov 2026 at 03:47:06, subject to the Cambridge Core terms of use, available at https://www.cambridge.org/core/terms. https://doi.org/10.1017/S0263574726104019

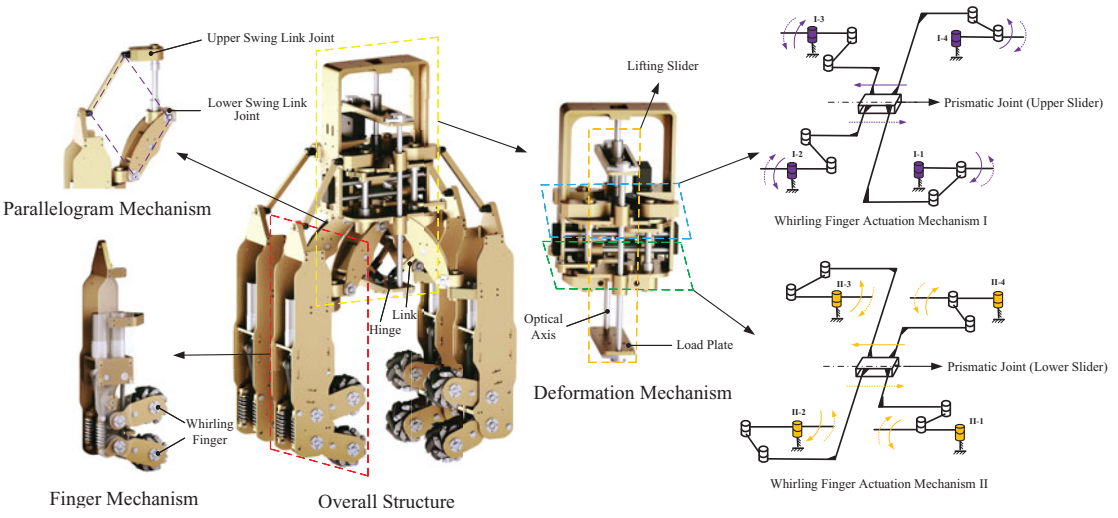


Figure 1. *Model and partial kinematic diagram of the ODH.*

lifting slider. Each slider has its own servo motor, which directly drives the rotation of the upper swing link joints **I-(1-4)** and the lower swing link joints **II-(1-4)**, respectively. This motion transmits through the parallelogram mechanism to synchronously adjust the posture and position of all four fingers, allowing the hand to adapt to objects of various shapes. The lifting slider includes an optical axis and a load plate. A dedicated servo motor drives the optical axis to raise or lower the load plate. This action, transmitted through hinged connections, lifts or flattens four connecting rods, thereby executing the hand's grasping and releasing motions. Each finger mechanism incorporates two whirling fingers with swing-rotation joints, designed for force-closure grasping of objects. Each whirling finger is equipped with an actively driven Mecanum wheel. Utilizing the friction generated between the object and the Mecanum wheel, the system achieves assisted grasping and in-hand posture adjustment of the object.

Compared with conventional multifingered hands with fixed fingertips, the omnidirectional wheel design provides a unique capability: active in-hand manipulation without regrasping. When the fingertips are in contact with a grasped object, the omnidirectional wheels can drive the object to rotate continuously about the grasping axis or translate within the grasp, without releasing or reconfiguring the fingers. In contrast, conventional multifingered hands with fixed fingertips must sequentially release and reposition their fingers to rotate an object (regrasping); this process interrupts force continuity and introduces the risk of dropping the object. This capability of the ODH is essential for tasks such as workpiece reorientation for assembly, surface inspection requiring continuous rotation, and precision positioning in confined spaces where arm mobility is limited. Although the wheel mechanism increases the hand's weight and mechanical complexity compared with fixed-fingertip designs, this trade-off is justified in applications where uninterrupted force control during in-hand manipulation is the primary requirement.

2.2. Forward kinematic model

In performing the kinematic analysis of the ODH, we use the modified Denavit–Hartenberg (M-D-H) method [25] for kinematic modeling. This method fixes the link coordinate system at the proximal end of each link. Since all four fingers are identical, we use Finger D to illustrate the forward kinematic model. Figure 2(a) establishes the coordinate system, with the base frame denoted as O_B-$x_By_Bz_B$. The motion of the lifting slider in Figure 1 can be equivalently described as the combined action of rotary joint 2 and rotary joint 3, with both joint angles undergoing an identical amount of change.

Based on the coordinate system established in Figure 2 and following the M-D-H modeling method, the parameter values for each link were determined, and the corresponding M-D-H parameter table is

Downloaded from https://www.cambridge.org/core. UNIVERSIDAD AUTONOMA METROPOLITANA, on 19 Nov 2026 at 03:47:06, subject to the Cambridge Core terms of use, available at https://www.cambridge.org/core/terms. https://doi.org/10.1017/S0263574726104019

Table II. *Parameters of the M-D-H method.*

i	α_{i-1}	a_{i-1}	d_i	θ_i	Range of θ_i
1	0	0	d_1	θ_1	0°∼−45°
2	90°	a_1	0	θ_2	105°∼135°
3	0	a_2	0	θ_3	180° $-\theta_2$
4	90°	a_3	0	θ_4	$-90°-\theta_1 \sim -\theta_1$
5	0	a_4	d_5	0	

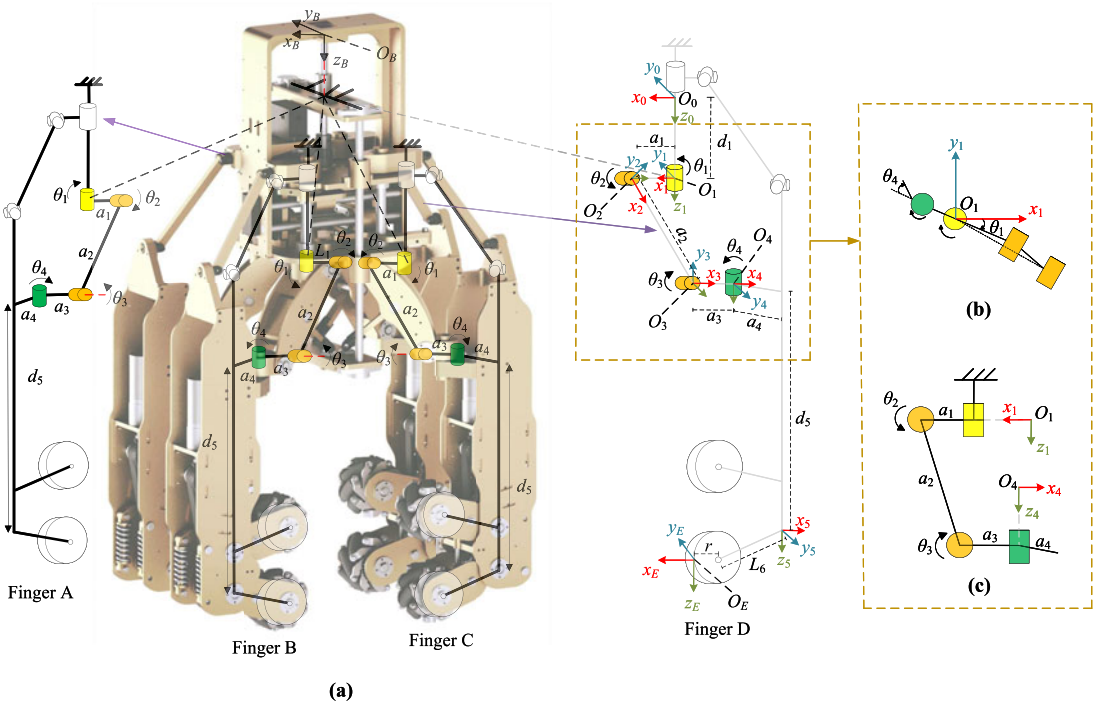


Figure 2. *(a) Coordinate system of the omnidirectional dexterous hand; (b) position of coordinate system O_4-$x_4y_4z_4$ in the x_1-O_1-z_1 plane; (c) position of coordinate system O_4-$x_4y_4z_4$ in the x_1-O_1-y_1 plane.*

presented in Table II. In the table, i denotes the joint number; α_{i-1} represents the rotation angle about axis x_{i-1} that aligns axis z_{i-1} with axis z_i; a_{i-1} indicates the displacement along axis x_{i-1} from axis z_{i-1} to axis z_i; θ_i is the rotation angle about axis z_i that brings axis x_{i-1} parallel to axis x_i; and d_i denotes the displacement along axis z_i from axis x_{i-1} to axis x_i.

According to the relationships defined above, the transformation matrix from coordinate system {i−1} to coordinate system {i} can be expressed as:

$$i^{i-1}\boldsymbol{T} = Rot(x, \alpha_{i-1}) \cdot Trans(\alpha_{i-1}, 0, 0) \cdot Rot(z, \theta_i) \cdot Trans(0, 0, d_i) \tag{1}$$

By multiplying the four matrices in Eq. (1), the general form of the transformation matrix $i^{i-1}\boldsymbol{T}$ can be obtained as follows:

$$i^{i-1}\boldsymbol{T} = \begin{bmatrix} c\theta_i & -s\theta_i & 0 & a_{i-1} \\ s\theta_i c\alpha_{i-1} & c\theta_i c\alpha_{i-1} & -s\alpha_{i-1} & -s\alpha_{i-1} d_i \\ s\theta_i s\alpha_{i-1} & c\theta_i s\alpha_{i-1} & c\alpha_{i-1} & c\alpha_{i-1} d_i \\ 0 & 0 & 0 & 1 \end{bmatrix} \tag{2}$$

where $c\theta_i$, $s\theta_i$, $c\alpha_{i-1}$ and $s\alpha_{i-1}$ denote $\cos\theta_i$, $\sin\theta_i$, $\cos\alpha_{i-1}$ and $\sin\alpha_{i-1}$, respectively.

Downloaded from https://www.cambridge.org/core. UNIVERSIDAD AUTONOMA METROPOLITANA, on 19 Nov 2026 at 03:47:06, subject to the Cambridge Core terms of use, available at https://www.cambridge.org/core/terms. https://doi.org/10.1017/S0263574726104019

Based on Eq. (2) and the parameters corresponding to each link coordinate system listed in Table II, the homogeneous transformation matrices between adjacent joint coordinate systems for Finger D are derived as ${}^{0}_{1}\boldsymbol{T}, {}^{1}_{2}\boldsymbol{T}, {}^{2}_{3}\boldsymbol{T}, {}^{3}_{4}\boldsymbol{T}, {}^{4}_{5}\boldsymbol{T}$. Consequently, the forward kinematic model of the dexterous hand is obtained as follows:

$$ {}^{B}_{E}\boldsymbol{T} = {}^{B}_{0}\boldsymbol{T} \cdot {}^{0}_{1}\boldsymbol{T} \cdot {}^{1}_{2}\boldsymbol{T} \cdot {}^{2}_{3}\boldsymbol{T} \cdot {}^{3}_{4}\boldsymbol{T} \cdot {}^{4}_{5}\boldsymbol{T} \cdot {}^{5}_{E}\boldsymbol{T} \tag{3} $$

where ${}^{B}_{0}\boldsymbol{T}$ represents the pose transformation matrix from coordinate system O_B-$x_By_Bz_B$ to the base coordinate system O_B-$x_By_Bz_B$, and ${}^{5}_{E}\boldsymbol{T}$ denotes the pose transformation matrix from coordinate system O_E-$x_Ey_Ez_E$ to the base coordinate system O_5-$x_5y_5z_5$.

2.3. Inverse kinematic model

Solving the inverse kinematics is a prerequisite for dexterous hand control, aiming to determine all joint angles based on the desired fingertip pose. We derive the inverse kinematic model using Finger D. To simplify the analysis, we introduce the coordinate system O_4-$x_4y_4z_4$ at Joint 4 as an intermediate reference frame. Consequently, the forward kinematic model can be reformulated as follows:

$$ {}^{B}_{E}\boldsymbol{T} = {}^{B}_{1}\boldsymbol{T} \cdot {}^{1}_{4}\boldsymbol{T} \cdot {}^{4}_{E}\boldsymbol{T} \tag{4} $$

where ${}^{B}_{1}\boldsymbol{T}$ denotes the homogeneous transformation matrix from coordinate system O_1-$x_1y_1z_1$ to the base coordinate system O_B-$x_By_Bz_B$. ${}^{1}_{4}\boldsymbol{T}$ represents the homogeneous transformation matrix from coordinate system O_4-$x_4y_4z_4$ to coordinate system O_1-$x_1y_1z_1$, and ${}^{4}_{E}\boldsymbol{T}$ is the homogeneous transformation matrix from the fingertip coordinate system O_E-$x_Ey_Ez_E$ to coordinate system O_4-$x_4y_4z_4$.

Let the fingertip pose of Finger D be given by:

$$ {}^{B}_{E}\boldsymbol{T} = \begin{bmatrix} n_x & o_x & a_x & p_x \\ n_y & o_y & a_y & p_y \\ n_z & o_z & a_z & p_z \\ 0 & 0 & 0 & 1 \end{bmatrix} \tag{5} $$

From Eq. (4), it follows that:

$$ {}^{1}_{4}\boldsymbol{T} = {}^{B}_{1}\boldsymbol{T}^{-1} \cdot {}^{B}_{E}\boldsymbol{T} \cdot {}^{4}_{E}\boldsymbol{T}^{-1} = \begin{bmatrix} n_x^{(4)} & o_x^{(4)} & a_x^{(4)} & p_x^{(4)} \\ n_y^{(4)} & o_y^{(4)} & a_y^{(4)} & p_y^{(4)} \\ n_z^{(4)} & o_z^{(4)} & a_z^{(4)} & p_z^{(4)} \\ 0 & 0 & 0 & 1 \end{bmatrix} \tag{6} $$

The coordinate system O_4-$x_4y_4z_4$ of Finger D in Figure 2(a) is analyzed in the x_1-O_1-z_1 plane and the x_1-O_1-y_1 plane, respectively. The resulting geometric relationships are shown in Figure 2(b) and (c). Based on the joint angles and link-length parameters indicated in Figure 2(b), the following can be derived:

$$ p_{x1} = L_1 + L_2\cos(\theta_{20} + \theta_2) + L_3\cos(\theta_{20} + \theta_2 + \theta_3) \tag{7} $$

$$ p_{z1} = L_2\sin(\theta_{20} + \theta_2) + L_3\sin(\theta_{20} + \theta_2 + \theta_3) \tag{8} $$

where p_{x1} and p_{z1} represent the projected coordinates of O_4 along the x_1-axis and z_1-axis, respectively, within the x_1-O_1-z_1 plane of the coordinate system O_1-$x_1y_1z_1$.

Downloaded from https://www.cambridge.org/core. UNIVERSIDAD AUTONOMA METROPOLITANA, on 19 Nov 2026 at 03:47:06, subject to the Cambridge Core terms of use, available at https://www.cambridge.org/core/terms. https://doi.org/10.1017/S0263574726104019

According to the joint angles and link-length parameters illustrated in Figure 2(c), the following can be obtained:

$$p_x^{(4)} = p_{x1}\cos\theta_1 - L_4\cos(\theta_1 + \theta_4) \tag{9}$$

$$p_y^{(4)} = p_{x1}\sin\theta_1 - L_4\sin(\theta_1 + \theta_4) \tag{10}$$

$$p_z^{(4)} = L_2\sin(\theta_{20} + \theta_2) \tag{11}$$

Combining Eq. (11) with the angular range of θ_2, and given that the variations of θ_2 and θ_3 are equal, θ_2 and θ_3 can be solved as:

$$\theta_3 = \theta_2 = \pi - \theta_{20} - \sin^{-1}\left(\frac{p_z^{(4)}}{L_2}\right) \tag{12}$$

To solve for θ_1 and θ_4, let $a = L_1 + L_2\cos(\theta_{20} + \theta_2) - L_3$. Squaring Eqs. (9) and (10), summing them, and simplifying yields the following expressions for θ_1 and θ_4:

$$\theta_1 = \varphi \pm \cos^{-1}\left(\frac{a^2 - {L_4}^2 + \left(p_x^{(4)}\right)^2 + \left(p_y^{(4)}\right)^2}{2aR}\right) \tag{13}$$

$$\theta_4 = \tan^{-1}\left(\frac{a\sin\theta_1 - p_y^{(4)}}{a\cos\theta_1 - p_x^{(4)}}\right) - \theta_1 \tag{14}$$

where $R = \sqrt{(p_x^{(4)})^2 + (p_y^{(4)})^2}$, $\varphi = \tan^{-1}\dfrac{p_y^{(4)}}{p_x^{(4)}}$.

2.4. Workspace analysis

The workspace serves as a critical metric for evaluating the dexterous hand's operational capability. It defines the set of all positions that the ODH fingertip can reach in space and can be dynamically adjusted through the deformation structure to achieve different grasping postures.

Based on the forward kinematic model established in Section 2.2 and the joint parameters listed in Table II, this section constructs the workspace of the dexterous hand by iterating over the feasible joint angles. The resulting spatial ranges in three dimensions as well as in each principal plane are illustrated in Figure 3.

Several typical grasping postures are presented for handling objects such as a sphere, a laterally placed cylinder, a vertically placed cylinder, and a cuboid (or planar object), as shown in Figure 4. In Figure 4, l denotes the vertical distance between the object center (O_C) and the lowest point of the load plate; l_w represents the longitudinal spacing between the wheels; l_{hw} indicates the lateral spacing between the wheels. r_{vc} and l_{vc} are the radius and length of the vertical cylinder, respectively; r_{sp} is the radius of the sphere; r_{hc} and l_{hc} are the radius and length of the horizontal cylinder, respectively. l_{cul}, l_{cuw}, and l_{cuh} correspond to the length, width, and height of the cuboid, respectively.

Based on the analysis of the ODH's workspace, combined with its geometric characteristics and dimensional boundaries, the allowable size ranges for grasping and pose adjustment are evaluated for the aforementioned objects, as summarized in Table III. This provides a theoretical foundation and geometric constraints for subsequent control-strategy design and the selection of object dimensions in experiments. In Table III, the symbol "—" under "Graspable size range" indicates that objects of any size within the geometric limits can be grasped; while "—" under "Adjustable pose size range" implies that the feasibility of pose adjustment depends on the specific adjustment task and must be considered accordingly.

Downloaded from https://www.cambridge.org/core. UNIVERSIDAD AUTONOMA METROPOLITANA, on 19 Nov 2026 at 03:47:06, subject to the Cambridge Core terms of use, available at https://www.cambridge.org/core/terms. https://doi.org/10.1017/S0263574726104019

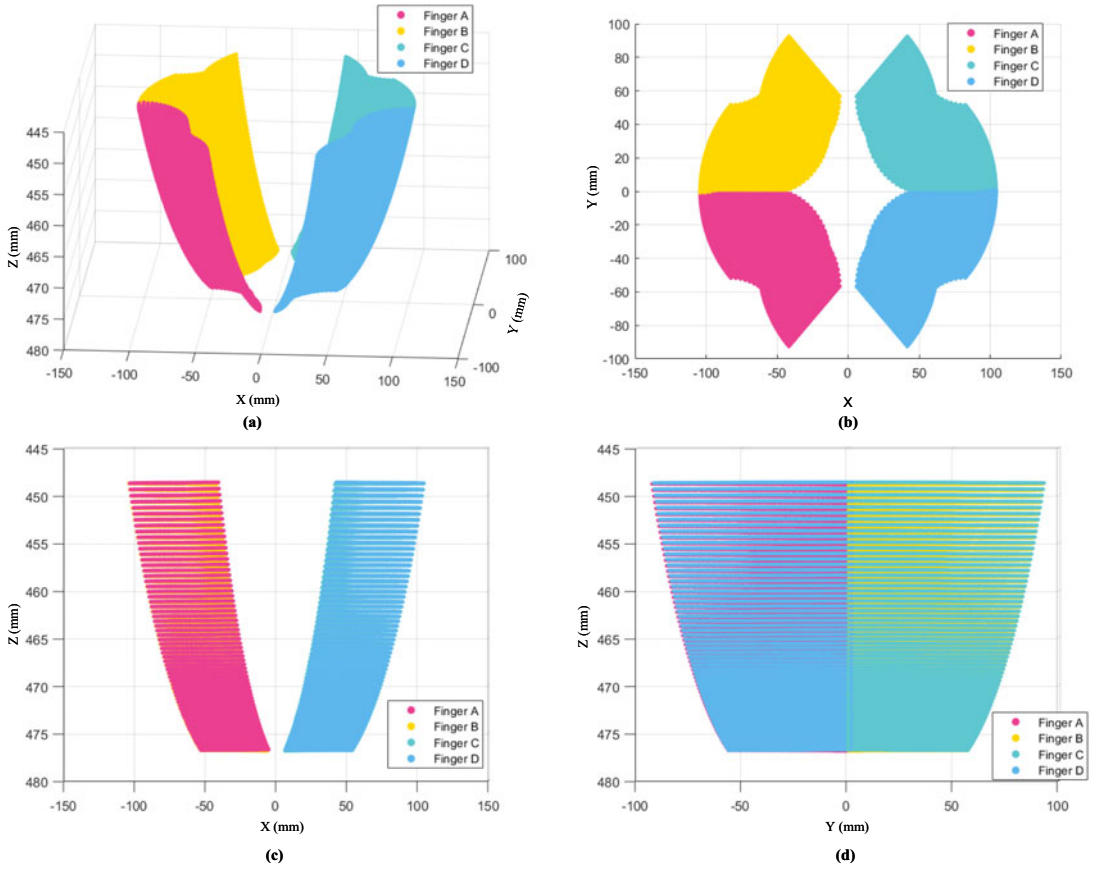


Figure 3. *(a) Three-dimensional workspace; (b) projection on the X-O-Y plane; (c) projection on the X-O-Z plane; (d) projection on the Y-O-Z plane.*

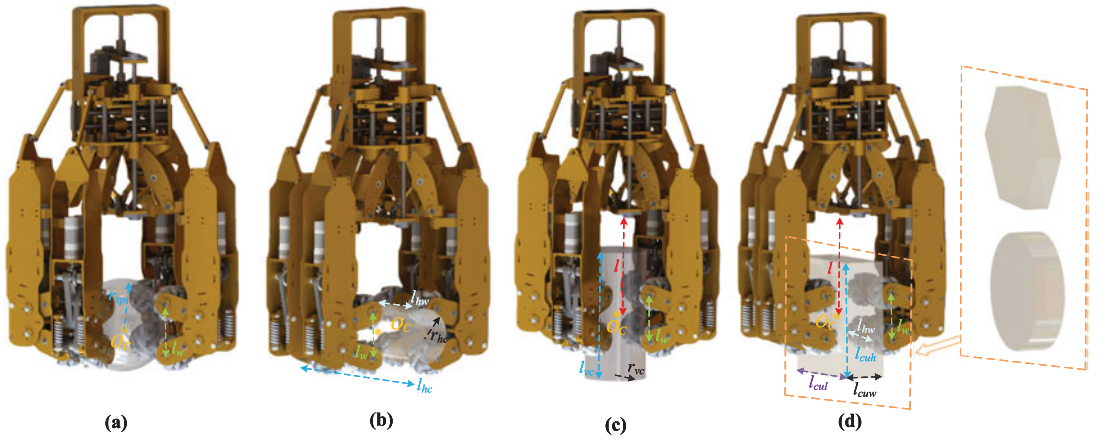


Figure 4. *Postures of the ODH grasping: (a) a sphere, (b) a horizontally oriented cylinder, (c) a vertically oriented cylinder, and (d) a cuboid (or a planar object).*

Downloaded from https://www.cambridge.org/core. UNIVERSIDAD AUTONOMA METROPOLITANA, on 19 Nov 2026 at 03:47:06, subject to the Cambridge Core terms of use, available at https://www.cambridge.org/core/terms. https://doi.org/10.1017/S0263574724104019

Table III. *Graspable object ranges.*

Object	Parameter	Graspable size range (mm)	Adjustable pose size range (mm)
Sphere	r_{sp}	53.6 ~ 104.2	53.6 ~ 104.2
Horizontally oriented cylinder	r_{hc}	53.6 ~ 104.2	53.6 ~ 104.2
	l_{hc}	—	l_{hw} ~ —
Vertically oriented cylinder	r_{vc}	53.6 ~ 104.2	53.6 ~ 104.2
	l_{vc}	—	l_w ~ —
Cuboid	l_{cul}	—	l_{hw} ~ —
	l_{cuw}	53.6 ~ 104.2	53.6 ~ 104.2
	l_{cuh}	—	l_w ~ —

3. Extended state observer–sliding mode admittance control

3.1. Admittance control model

When the dexterous hand interacts with an object, AC establishes the virtual spring-mass-damper model for the fingertip wheels. Based on a given desired contact force, this model adjusts the desired position of the fingertip. Within the AC framework, the contact model between the fingertip of the dexterous hand and the external object is expressed as:

$$\boldsymbol{M}\left(\ddot{\boldsymbol{X}}_r - \ddot{\boldsymbol{X}}_d\right) + \boldsymbol{D}\left(\dot{\boldsymbol{X}}_r - \dot{\boldsymbol{X}}_d\right) + \boldsymbol{K}\left(\boldsymbol{X}_r - \boldsymbol{X}_d\right) = \boldsymbol{F}_d - \boldsymbol{F} \tag{15}$$

where $\boldsymbol{M}$, $\boldsymbol{D}$, and $\boldsymbol{K}$ represent the virtual mass matrix, virtual damping matrix, and virtual stiffness matrix of the admittance model, respectively; $\boldsymbol{X}_r$, $\dot{\boldsymbol{X}}_r$, and $\ddot{\boldsymbol{X}}_r$ denote the reference position, velocity, and acceleration of the dexterous hand; $\boldsymbol{X}_d$, $\dot{\boldsymbol{X}}_d$, and $\ddot{\boldsymbol{X}}_d$ are the desired position, velocity, and acceleration; and $\boldsymbol{F}_d$ and $\boldsymbol{F}$ stand for the desired grasping force and the environmental interaction force, respectively.

In the ODH grasping configuration, the four fingers are arranged symmetrically around the object, and the deformation mechanism synchronously adjusts all fingertip positions. Once the hand has adapted to the object geometry, the dominant interaction occurs along the grasping direction. Under the assumption of symmetric contact, the off-diagonal coupling terms in the stiffness and damping matrices are negligible, and the multidimensional admittance dynamics can be decoupled into independent one-dimensional systems along each contact axis. This decoupling is a common practice in grasp force control when the contact geometry is well-conditioned [21, 27]. Accordingly, this paper focuses on a one-dimensional interactive system along the primary grasping direction, and the admittance model Eq. (15) reduces to:

$$M\left(\ddot{x}_r - \ddot{x}_d\right) + D\left(\dot{x}_r - \dot{x}_d\right) + K\left(x_r - x_d\right) = F_d - F \tag{16}$$

The influence of the tangential friction forces generated during active Mecanum wheel rotation also warrants discussion. When the wheels are driven to rotate or reposition the object, each wheel exerts a tangential friction force on the object surface. This tangential component acts in the plane perpendicular to the primary grasping direction, while the normal contact force acts along the grasping direction. Due to the symmetric arrangement of the four fingers and the orthogonal relationship between these two directions, the tangential friction force does not directly enter the force balance along the grasping direction to the first order.

However, tangential wheel motion may indirectly perturb the normal force channel through roller contact discontinuities on the Mecanum wheel surface, geometric asymmetries in the grasp, and friction-induced normal force fluctuations. These effects are bounded by the wheel motor torque limit. In this study, the wheels are actuated for object pose adjustment during grasping, rather than for high-speed continuous rotation. Under this operating condition, such perturbations are treated as part of the lumped

Downloaded from https://www.cambridge.org/core. UNIVERSIDAD AUTONOMA METROPOLITANA, on 19 Nov 2026 at 03:47:06, subject to the Cambridge Core terms of use , available at https://www.cambridge.org/core/terms. https://doi.org/10.1017/S0263574726104019

disturbance term Δ in the sliding mode dynamics and are compensated by the ESO and the sliding mode control term.

It should be noted that the one-dimensional decoupling assumption is predicated on the grasping configurations and manipulation tasks addressed in this work. Under strongly asymmetric grasps or conditions involving significant tangential contact forces beyond those considered here, a multidimensional coupled contact model would be required. This extension is identified as a direction for future work.

In the admittance model, x_d is constant or varies slowly; thus, $\dot{x}_d = 0$ and $\ddot{x}_d = 0$. During grasping, the desired position x_d corresponding to the desired grasping force F_d cannot be directly measured. In most AC, the virtual stiffness term $K(x_r - x_d)$ serves a dual purpose: it maps the force error to a position correction, and it drives the end-effector toward a desired absolute position x_d. However, during grasping, the desired position x_d that corresponds to a given desired force F_d depends on the object's geometry and material stiffness. Since the object properties are generally unknown, x_d cannot be accurately specified. Furthermore, if the virtual stiffness K does not match the true environmental stiffness, a steady-state force error inevitably arises. Many existing methods address this mismatch by estimating the environmental stiffness and adjusting the admittance parameters accordingly; however, this requires accurate identification.

In this work, we adopt a different strategy. Rather than estimating the environment to make the stiffness term work, we remove the stiffness term entirely. Our objective is accurate force tracking during sustained contact, not regulation to a specific absolute position. In this context, the stiffness term is unnecessary: the virtual damping D provides sufficient control over the transient response, and the SMC term u_{smc} (introduced in Section 3.2) ensures robust steady-state accuracy without requiring knowledge of the environmental stiffness. Setting $K = 0$ eliminates both the dependence on x_d and the risk of steady-state error due to stiffness mismatch. This strategy, of course, would not be appropriate if the task required the hand to return to a specific position after force release. In the present work, however, the primary objective is stable force tracking during grasping, for which $K = 0$ is a deliberate and well-motivated design choice.

Consequently, we set $K = 0$, and the admittance model simplifies to:

$$M\ddot{x}_r + D\dot{x}_r = F_d - F \tag{17}$$

where x_r represents the reference trajectory sent to the underlying position controller. Defining the force error as $e_F = F_d - F$, the reference acceleration $\ddot{x}_r$ required by the position controller can be solved as follows:

$$\ddot{x}_r = \frac{1}{M}\left[-D\dot{x}_r + e_F\right] \tag{18}$$

In a practical discrete-time system, $\ddot{x}_r$ is integrated to obtain the reference velocity $\dot{x}_r$, and $\dot{x}_r$ is further integrated to yield the position correction Δx. Let x_0 denote the hand position at the initial contact with the object. The final reference position is then given by $x_r = x_0 + \Delta x$. The underlying position controller drives the actual hand position x to track the continuously updated x_r, thereby achieving grasping with the desired force.

3.2. Sliding mode admittance control

Equations (17) and (18) describe a second-order system, in which the dynamic behavior of the force error is entirely governed by the virtual mass M and damping D. When the mechanical properties of the grasped object are unknown or vary, the performance of this controller may degrade, manifesting as steady-state errors in force tracking, overshoot, or oscillations.

Sliding mode control (SMC) is a highly robust nonlinear control method that can force the system state to remain on a predefined sliding surface despite parameter uncertainties and disturbances. Therefore, this paper introduces a sliding-mode control term u_{smc} into the admittance framework to enhance the system's adaptability to different objects. Accordingly, Eqs. (17) and (18) are reformulated

Downloaded from https://www.cambridge.org/core. UNIVERSIDAD AUTONOMA METROPOLITANA, on 19 Nov 2026 at 03:47:06, subject to the Cambridge Core terms of use, available at https://www.cambridge.org/core/terms. https://doi.org/10.1017/S0263574726104019

as follows:

$$M\ddot{x}_r + D\dot{x}_r = F_d - F + u_{smc} \tag{19}$$

$$\ddot{x}_r = \frac{1}{M}\left(-D\dot{x}_r + e_F + u_{smc}\right) \tag{20}$$

The sliding surface is defined using the force error and its derivative:

$$s = \dot{e}_F + \lambda e_F \tag{21}$$

where $\lambda > 0$ represents the convergence rate of the system response to errors. When the system state is constrained to the sliding surface $s = 0$, the following relation holds: $\dot{e}_F + \lambda e_F = 0$. This homogeneous differential equation has the solution: $e_F(t) = e_F(0)e^{-\lambda t}$, which indicates that the force error converges to zero exponentially at the rate λ. The convergence behavior is deterministic and independent of the system parameters.

To apply SMC, two necessary conditions must be satisfied. First, the system must have a well-defined relative degree with respect to the chosen sliding variable, such that the control input appears explicitly in its derivative. Second, the matched uncertainty condition must hold, meaning that parameter uncertainties and external disturbances enter the system through the same channel as the control input, allowing the sliding mode term to compensate for them. We verify these conditions as follows.

Relative degree analysis. From the sliding surface definition $s = \dot{e}_F + \lambda e_F$ in (21), we compute its time derivative:

$$\dot{s} = \ddot{e}_F + \lambda \dot{e}_F \tag{22}$$

With $e_F = F_d - F$ and F_d constant, $\dot{e}_F = -\dot{F}$ and $\ddot{e}_F = -\ddot{F}$. In physical grasping, when the dexterous hand makes contact with an object, the object deforms elastically and exerts a reaction force on the fingertips. The true stiffness of any real object is strictly positive ($K_e > 0$); otherwise, no contact force would arise. In practice, however, the exact stiffness value is rarely known, as it depends on the object's material and geometry. For simulation purposes, an explicit contact model is required to generate a realistic interaction force between the hand and a virtual object. For analytical derivation, a structural relationship between the force and the relative motion is also necessary. To serve both purposes, we adopt the widely used contact model $F = K_e(x - x_e)$ [26], where K_e denotes the unknown environmental stiffness and x_e is the position of the object surface. It is important to emphasize that our controller design does not require the numerical value of K_e. The model is introduced in the theoretical analysis solely to establish the structural relationship between the contact force and the hand position.

We have $\ddot{F} \approx K_e\ddot{x}_r$ under the assumption that the inner position controller ensures $\ddot{x} = \ddot{x}_r$. Substituting the admittance dynamics Eq. (20), we obtain:

$$\ddot{e}_F = -\frac{K_e}{M}\left(-D\dot{x}_r + e_F + u_{smc}\right) \tag{23}$$

Therefore,

$$\dot{s} = -\Gamma\left(-D\dot{x}_r + e_F + u_{smc}\right) - \lambda\dot{F} + \Delta \tag{24}$$

Since the environmental stiffness $K_e > 0$ and the virtual mass $M > 0$, the coefficient of u_{smc} in $\dot{s}$ is $\Gamma = \frac{K_e}{M} > 0$. Hence, the control input u_{smc} appears in the first derivative of s, establishing that the system has a relative degree of 1 with respect to the sliding variable. This satisfies the first necessary condition for the SMC.

Matched uncertainty condition. This condition is verified by expanding and regrouping the terms in Eq. (24), which yields:

$$\dot{s} = \left(\Gamma D\dot{x}_r - \Gamma e_F - \lambda\dot{F} + \Delta\right) - \Gamma u_{smc} \tag{25}$$

where $\Gamma = \frac{K_e}{M} > 0$, and Δ lumps estimation errors, model uncertainties, and other residual terms. The above expression shows that the total disturbance and the control input u_{smc} enter the $\dot{s}$ dynamics through

Downloaded from https://www.cambridge.org/core. UNIVERSIDAD AUTONOMA METROPOLITANA, on 19 Nov 2026 at 03:47:06, subject to the Cambridge Core terms of use, available at https://www.cambridge.org/core/terms. https://doi.org/10.1017/S0263574726104019

an additive channel with a nonzero coefficient $\Gamma \neq 0$. Hence, the matched uncertainty condition is satisfied.

3.3. State estimation based on an ESO

However, this method relies on the accurate acquisition of the derivative of the force error, $\dot{e}_F$. In practical systems, the measured contact force, $F_m(t) = F(t) + \nu(t)$, inevitably contains noise $\nu(t)$. Direct numerical differentiation of a noisy signal will severely amplify the noise, leading to significant fluctuations in the computed sliding surface and inducing high-frequency chattering in the control input u_{smc}. To address this issue, an ESO is introduced to estimate both the state of the force-error system and the total disturbance, thereby reconstructing the sliding surface.

Treating e_F as the output of a second-order system, the state variables are defined as: $z_1 = e_F$, $z_2 = \dot{e}_F$. Owing to measurement noise and system uncertainties—such as unknown environmental stiffness and other unmodeled dynamics—the total disturbance is extended as an additional state variable z_3. Its rate of change is assumed to be bounded; i.e., there exists a constant $L > 0$ such that $\dot{z}_3 = h(t), |\, h(t) \,| \leq L$. Consequently, the extended-state system is obtained as follows:

$$\begin{cases} \dot{z}_1 = z_2 \\ \dot{z}_2 = z_3 \\ \dot{z}_3 = h(t) \\ y = z_1 + \nu(t) \end{cases} \tag{26}$$

where $y = e_{F,m}$ denotes the measurable (noisy) force error, and $\nu(t)$ represents the measurement noise. In this work, $\nu(t)$ is assumed to be bounded, $|\, \nu(t) \,| \leq \nu_{\max}$ for some constant $\nu_{\max} > 0$. This is a mild assumption in practical robotic systems.

Observability analysis. Before proceeding with the observer design, it is necessary to verify that the extended state system (26) is observable. Neglecting the noise term $\nu(t)$ and the disturbance derivative $h(t)$, the noise-free part of system (26) can be written in the linear canonical form:

$$\dot{\boldsymbol{z}} = \boldsymbol{A}_o \boldsymbol{z}, y = \boldsymbol{C}_o \boldsymbol{z} \tag{27}$$

where $\boldsymbol{z} = [\mathrm{z}_1, \mathrm{z}_2, \mathrm{z}_3]^T$, $\boldsymbol{A}_o = \begin{bmatrix} 0 & 1 & 0 \\ 0 & 0 & 1 \\ 0 & 0 & 0 \end{bmatrix}$, $\boldsymbol{C}_o = [\,1 \quad 0 \quad 0\,]$. The observability matrix for this system is

$$\mathcal{O} = \begin{bmatrix} \boldsymbol{C}_o \\ \boldsymbol{C}_o \boldsymbol{A}_o \\ \boldsymbol{C}_o \boldsymbol{A}_o^2 \end{bmatrix} = \begin{bmatrix} 1 & 0 & 0 \\ 0 & 1 & 0 \\ 0 & 0 & 1 \end{bmatrix} \tag{28}$$

Since the observability matrix $\mathcal{O}$ is the identity matrix with rank equal to the state dimension of three, the extended state system is fully observable. For system (26), an ESO is designed as follows:

$$\begin{cases} \dot{\hat{z}}_1 = \hat{z}_2 + \beta_1 \left(y - \hat{z}_1 \right) \\ \dot{\hat{z}}_2 = \hat{z}_3 + \beta_2 \left(y - \hat{z}_1 \right) \\ \dot{\hat{z}}_3 = \beta_3 \left(y - \hat{z}_1 \right) \end{cases} \tag{29}$$

where $\hat{z}_1$, $\hat{z}_2$, and $\hat{z}_3$ denote the estimates of z_1, z_2, and z_3, respectively, and $\beta_1, \beta_2, \beta_3 > 0$ are observer gains to be designed. Define the observer errors as $\tilde{z}_i = z_i - \hat{z}_i$ for $i = 1, 2, 3$. The error dynamics are

Downloaded from https://www.cambridge.org/core. UNIVERSIDAD AUTONOMA METROPOLITANA, on 19 Nov 2026 at 03:47:06, subject to the Cambridge Core terms of use, available at https://www.cambridge.org/core/terms. https://doi.org/10.1017/S0263574726104019

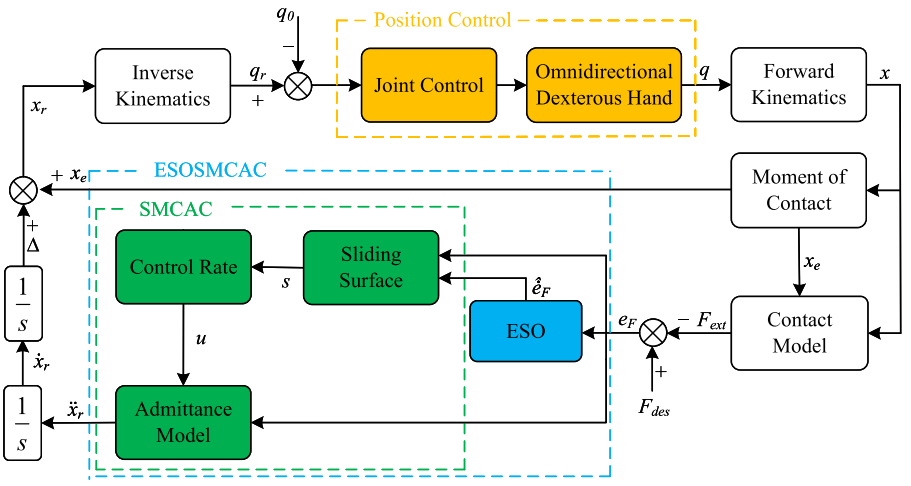


Figure 5. *System control block diagram.*

derived from Eqs. (26) and (29) as follows:

$$\begin{cases} \dot{\tilde{z}}_1 = \dot{z}_1 - \dot{\hat{z}}_1 = \tilde{z}_2 - \beta_1 \tilde{z}_1 - \beta_1 \nu\,(t) \\ \dot{\tilde{z}}_2 = \dot{z}_2 - \dot{\hat{z}}_2 = \tilde{z}_3 - \beta_2 \tilde{z}_1 - \beta_2 \nu\,(t) \\ \dot{\tilde{z}}_3 = \dot{z}_3 - \dot{\hat{z}}_3 = h\,(t) - \beta_3 \tilde{z}_1 - \beta_3 \nu\,(t) \end{cases} \tag{30}$$

Neglecting the transient effects of measurement noise $\nu(t)$ and disturbance dynamics $h(t)$, consider the homogeneous equation of the observer error:

$$\begin{bmatrix} \dot{\tilde{z}}_1 \\ \dot{\tilde{z}}_2 \\ \dot{\tilde{z}}_3 \end{bmatrix} = \boldsymbol{A} \begin{bmatrix} \tilde{z}_1 \\ \tilde{z}_2 \\ \tilde{z}_3 \end{bmatrix}, \ \boldsymbol{A} = \begin{bmatrix} -\beta_1 & 1 & 0 \\ -\beta_2 & 0 & 1 \\ -\beta_3 & 0 & 0 \end{bmatrix} \tag{31}$$

The characteristic polynomial of Eq. (31) is

$$\det\,(s\boldsymbol{I} - \boldsymbol{A}) = \det \begin{bmatrix} s + \beta_1 & -1 & 0 \\ \beta_2 & s & -1 \\ \beta_3 & 0 & s \end{bmatrix} = s^3 + \beta_1 s^2 + \beta_2 s + \beta_3 \tag{32}$$

where $\boldsymbol{I}$ is the identity matrix. To simplify parameter tuning, the observer poles are all placed at $-\omega_o$, with $\omega_o > 0$ representing the observer bandwidth. The desired characteristic polynomial is

$$(s + \omega_o)^3 = s^3 + 3\omega_o s^2 + 3\omega_o^2 s + \omega_o^3 \tag{33}$$

Consequently, the observer gains are obtained as: $\beta_1 = 3\omega_o, \beta_2 = 3\omega_o^2, \beta_3 = \omega_o^3$. Thus, the dynamic performance of the observer can be tuned via the single parameter ω_o. Using the estimate $\hat{z}_2 = \widehat{\hat{e}_F}$ provided by the ESO, the sliding surface is reconstructed as:

$$s = \widehat{\hat{e}_F} + \lambda e_F = \hat{z}_2 + \lambda e_F \tag{34}$$

The system control block diagram is shown in Figure 5.

Downloaded from https://www.cambridge.org/core. UNIVERSIDAD AUTONOMA METROPOLITANA, on 19 Nov 2026 at 03:47:06, subject to the Cambridge Core terms of use, available at https://www.cambridge.org/core/terms. https://doi.org/10.1017/S0263574726104019

3.4. Stability analysis

A stability analysis of the proposed ESOSMCAC strategy is performed using the direct Lyapunov method. Consider the Lyapunov function candidate:

$$V = \frac{1}{2}s^2 \tag{35}$$

Clearly, $V \geq 0$, and the function is positive definite. Differentiating V and substituting Eq. (24), the sliding mode control law is designed as $u_{smc} = \rho \cdot \text{sgn}(s)$, where $\text{sgn}(s)$ is the signum function. Consequently, we obtain:

$$\dot{V} = s\dot{s} = -\Gamma s\Psi - \Gamma\rho \mid s \mid \tag{36}$$

where $\Psi = -D\dot{x}_r + e_F - \frac{\lambda}{\Gamma}\dot{F} + \frac{\Delta}{\Gamma}$. The term Ψ consists of four components, each bounded under normal grasping conditions. The damping term $-D\dot{x}_r$ is bounded because the reference velocity remains finite during contact. The force error e_F is regulated by the closed-loop controller. The force derivative term $-\frac{\lambda}{\Gamma}\dot{F}$ is bounded under physical contact with finite stiffness, since $\dot{F} = K_e\dot{x}$ with bounded hand velocity and finite K_e. The residual term $\frac{\Delta}{\Gamma}$ encapsulates ESO estimation errors and unmodeled dynamics, which are bounded due to the proven convergence of the ESO. Therefore, there exists a constant $\rho_0 > 0$ such that $\mid \Psi \mid \leq \rho_0$ for all time t. Designing the control gain as $\rho = \rho_0 + \frac{\eta_0}{\Gamma}$, $\eta_0 > 0$, and using the absolute-value inequality: $-s\Psi \leq \mid s \mid\mid \Psi \mid \leq \mid s \mid \rho_0$, we obtain:

$$\dot{V} \leq \Gamma\rho_0 \mid s \mid -\Gamma\,(\rho_0 + \eta_0/\,\Gamma) \mid s \mid = -\eta_0 \mid s \mid \leq 0 \tag{37}$$

Remark on the uncertainty in $\Gamma = \frac{K_e}{M}$. The parameter Γ involves the environmental stiffness K_e, which is unknown and may vary during grasping. The stability proof does not require Γ to be constant or precisely known, only that $\Gamma > 0$ (guaranteed by $K_e > 0$ for any real object) and that Γ remains bounded within a finite range for a given object.

Equation (37) shows that the system is stable in the Lyapunov sense and satisfies the finite-time reaching condition of sliding-mode control, guaranteeing that the system state will reach the sliding surface $s = 0$ in finite time and that the force error will converge exponentially. However, the sign function $\text{sgn}(s)$ induces high-frequency chattering. To mitigate this effect, a continuous saturation function such as the hyperbolic tangent is commonly employed:

$$u_{\text{smc}} = \rho \cdot \tanh\left(\frac{s}{\phi}\right) \tag{38}$$

where $\phi > 0$ is the boundary layer thickness. This continuous approximation creates a thin boundary layer around the sliding surface. When $\mid s \mid > \phi$, the tanh function saturates and behaves approximately like the ideal signum function, preserving strong robustness. When $\mid s \mid \leq \phi$, the control law degenerates into a linear proportional control $u_{smc} \approx \rho \cdot \frac{s}{\phi}$, providing smooth regulation within the boundary layer.

It should be noted that with the continuous tanh function, the strict finite-time reaching condition no longer holds. Instead, the system converges asymptotically. Specifically, the system state enters the boundary layer region $\mid s \mid \leq \phi$ in finite time, after which it converges asymptotically to a small neighborhood of the sliding surface $s \approx 0$. This represents a practical engineering trade-off: by sacrificing strict finite-time convergence, the control input becomes smooth and chattering is effectively suppressed.

Regarding practical implementation, actuator dynamics and communication delays can potentially excite chattering in sliding-mode controllers even when a continuous saturation function is used. In this work, the total loop delay—comprising sensor latency, controller computation, communication, and actuator response—is significantly shorter than the time constant of the admittance dynamics, ensuring that the controller responds to force variations before significant error accumulates. Moreover, because the tanh function replaces the discontinuous switching of the signum function with smooth linear feedback within the boundary layer, the control action is less susceptible to the repeated zero-crossing oscillations that would otherwise be induced by delays.

Downloaded from https://www.cambridge.org/core. UNIVERSIDAD AUTONOMA METROPOLITANA, on 19 Nov 2026 at 03:47:06, subject to the Cambridge Core terms of use, available at https://www.cambridge.org/core/terms. https://doi.org/10.1017/S0263574726104019

4. Simulations and experiments

To verify the effectiveness and superiority of the proposed ESOSMCAC approach, tests were conducted both in simulation and on a physical experimental platform. Based on the experimental data from Finger D, the method was evaluated in terms of force-control accuracy, convergence speed, and system stability under unknown stiffness conditions.

4.1. Simulations

A simulation environment was built in Matlab/Simulink. Based on the contact model, three control strategies are implemented and compared for desired force grasping of objects with unknown environmental stiffness: the AC from Eq. (17), the sliding-mode admittance control (SMCAC) incorporating Eq. (21), and the ESOSMCAC incorporating Eq. (34).

Four simulation cases were first designed without measurement noise to evaluate the baseline force tracking performance under different stiffness and desired force conditions: (A) $K_e = 3$ N/mm, $F_d = 10$ N; (B) $K_e = 3$ N/mm, $F_d = 20$ N; (C) $K_e = 5$ N/mm, $F_d = 10$ N; (D) $K_e = 5$ N/mm, $F_d = 20$ N.

The admittance parameters were identical for all three methods: virtual mass $m = 1$, damping coefficient $d = 3$. For SMCAC and ESOSMCAC, the sliding-mode parameters were set to $\lambda = 5$, sliding gain $\rho = 10$, and boundary-layer thickness $\phi = 1$. In ESOSMCAC, the observer bandwidth was chosen as $\omega_o = 50$. These are tuned according to the following rationale. The parameter λ governs the exponential decay rate of the force error on the sliding surface. A larger λ accelerates convergence but amplifies the contribution of force measurement noise to the sliding variable. The gain ρ must dominate the lumped uncertainty bound to satisfy the reaching condition. It is tuned by gradually increasing from a small value until overshoot or oscillation appears in the force response, then slightly reduced. The parameter ϕ controls the trade-off between chattering suppression and tracking accuracy. A smaller ϕ yields higher accuracy but increases control activity; a larger ϕ smooths the control signal at the expense of a wider steady-state error bound. The parameter ω_o is the sole tuning parameter of the ESO. The bandwidth ω_o governs a fundamental trade-off: a higher bandwidth enables the observer to estimate the force error derivative and the total disturbance more rapidly, which in turn allows faster sliding surface reconstruction and more timely disturbance compensation; however, it also amplifies the high-frequency measurement noise, degrading the smoothness of the reconstructed sliding surface and increasing control chattering. Conversely, a lower bandwidth provides stronger noise attenuation but slows down the estimation dynamics, which delays the sliding surface reconstruction and reduces force tracking accuracy. Accordingly, the parameters are adjusted based on the desired control performance and selected through several numerical simulations.

During the initial stage, the ODH approaches the object at a constant velocity. Contact occurs at $t = 3$s, after which the admittance-based control phase begins. The resulting force-control and position-tracking performances are shown in Figure 6(a)–(d). To quantitatively compare the three controllers, the 5% settling time and the mean absolute error (MAE) in steady state are evaluated for all nine cases. The settling time is defined as the time after contact at which the force error enters and remains within $\pm 5\%$ of the desired force. The MAE is computed over the steady-state interval after the transient response has settled. The results for cases (A)–(D) are summarized in Table IV.

To validate the noise rejection capability of the ESO and the robustness of the proposed method under more realistic conditions, five simulation cases with measurement noise are designed. In all five cases, Gaussian white noise with a standard deviation (SD) of 0.2 N is added to the measured contact force, representing the ripple observed in the force sensor signals on the experimental platform.

Cases E and F evaluate the force tracking performance in the presence of sensor noise under two stiffness conditions ($K_e = 3$ N/mm and 5 N/mm, respectively), both with $F_d = 10$ N. The resulting force-control and position-tracking performances are shown in Figure 6(e)–(f). The results for cases (E)–(F) are summarized in Table IV.

The results of the six simulation cases demonstrate that the ESOSMCAC method significantly outperforms both the AC and SMCAC methods. In terms of force control, SMCAC and ESOSMCAC track the

Downloaded from https://www.cambridge.org/core. UNIVERSIDAD AUTONOMA METROPOLITANA, on 19 Nov 2026 at 03:47:06, subject to the Cambridge Core terms of use, available at https://www.cambridge.org/core/terms. https://doi.org/10.1017/S0263574726104019

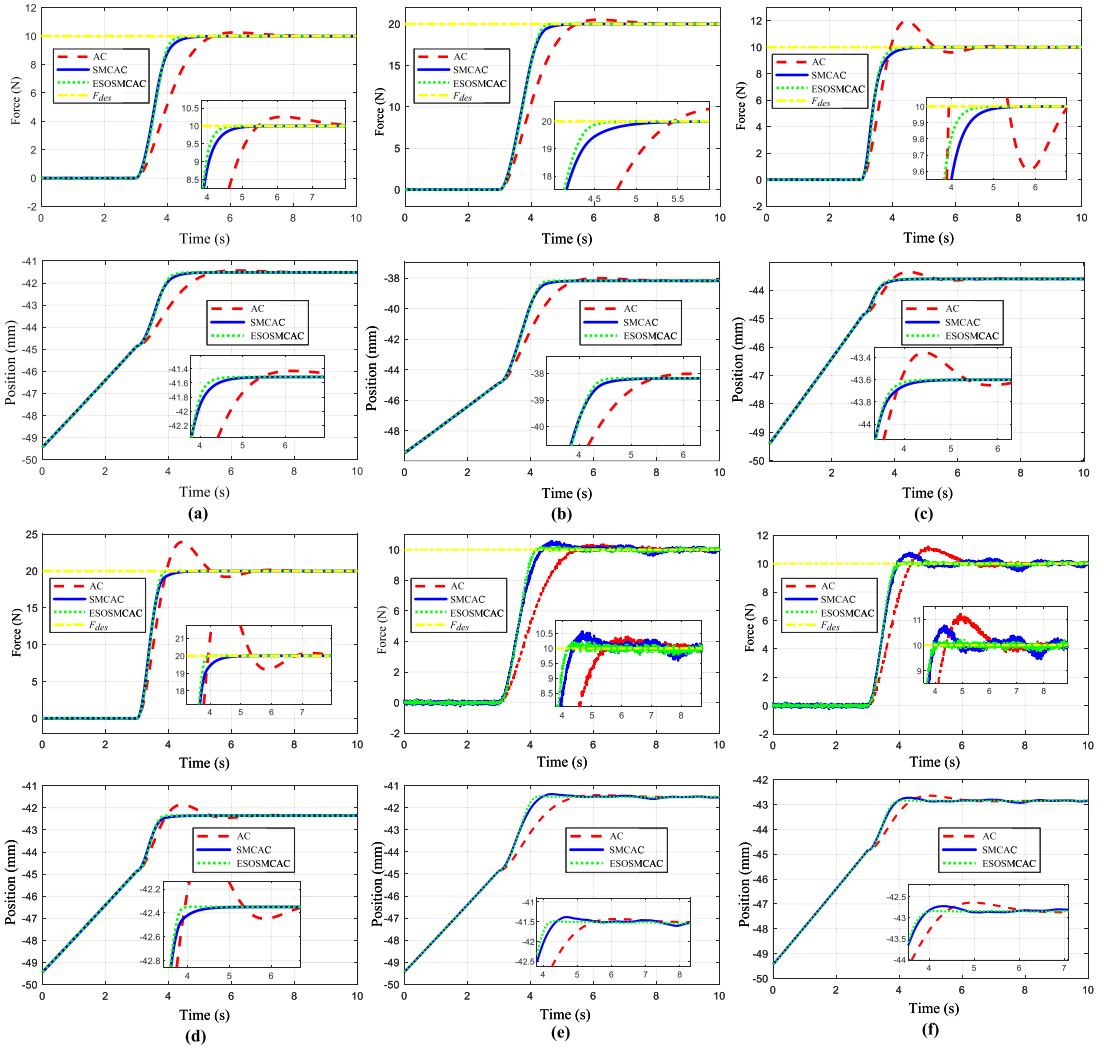


Figure 6. *Force control and position tracking simulation results for the three methods. Subfigures (a)–(d) correspond to the noise-free cases (A)–(D), respectively. Subfigures (e)–(f) correspond to the noisy cases (E)–(F).*

desired force more closely, exhibiting smaller steady-state errors and lower oscillation amplitudes across objects of different stiffnesses. However, ESOSMCAC achieves the best performance: its steady-state force error is reduced by approximately 37.8–57.9% compared to SMCAC and by about 16.3–90.6% compared to AC. In contrast, AC shows poor adaptability to varying stiffnesses, resulting in the largest force-control deviations. Regarding position response, both SMCAC and ESOSMCAC maintain smooth position tracking, while the position response of AC exhibits noticeable oscillations due to its larger force errors. In terms of convergence speed, the settling-time ranking is ESOSMCAC < SMCAC < AC. Specifically, ESOSMCAC reduces the settling time by approximately 6.2–50.9% compared to SMCAC and by about 38.6–70.7% compared to AC. These results fully validate the superiority of ESOSMCAC in balancing convergence speed with force-control accuracy when the object stiffness is unknown.

Downloaded from https://www.cambridge.org/core. UNIVERSIDAD AUTONOMA METROPOLITANA, on 19 Nov 2026 at 03:47:06, subject to the Cambridge Core terms of use , available at https://www.cambridge.org/core/terms. https://doi.org/10.1017/S0263574726104019

Table IV. *Quantitative performance comparison of the three controllers across cases (A)–(F).*

Case	Controller	5% Settling time (s)	Steady-state mean absolute error (N)
A	AC	2.085	0.0973
	SMCAC	1.245	0.0248
	ESOSMCAC	1.085	0.0143
B	AC	2.085	0.1950
	SMCAC	1.365	0.0463
	ESOSMCAC	1.280	0.0195
C	AC	2.675	0.0641
	SMCAC	1.070	0.0246
	ESOSMCAC	0.900	0.0153
D	AC	2.675	0.1283
	SMCAC	1.035	0.0460
	ESOSMCAC	0.945	0.0120
E	AC	2.120	0.1197
	SMCAC	1.220	0.1267
	ESOSMCAC	1.065	0.0675
F	AC	2.795	0.0835
	SMCAC	1.670	0.1274
	ESOSMCAC	0.820	0.0699

Cases G and H test the disturbance rejection capability against sudden external forces. In each case, an external force of 5 N is abruptly applied at $t = 8$ s and removed at $t = 11$ s, simulating an unexpected contact or collision during grasping. Case G uses $K_e = 3$ N/mm, and Case H uses $K_e = 5$ N/mm, both with $F_d = 10$ N. Case I evaluates the robustness to time-varying environmental stiffness, a scenario that may arise when grasping objects with non-uniform internal structure or when the contact condition changes during in-hand posture adjustment. The desired force is maintained at $F_d = 10$ N, while the stiffness varies over time: $K_e = 3$ N/mm during $t = 0$–7 s, $K_e = 6$ N/mm during $t = 7$–11 s, and $K_e = 2$ N/mm during $t = 11$–15 s. These cases examine whether the controller can reject the disturbance and restore the desired grasping force without overshoot or instability. The force control and position tracking performance for the noisy and disturbed cases (G)–(I) are shown in Figure 7. The 5% settling time and steady-state MAE for cases (G)–(I) are summarized in Table V.

Without the ESO, AC and SMCAC rely on direct numerical differentiation of the noisy force signal to compute the force error derivative, which amplifies the noise and leads to high-frequency fluctuations in the control input. ESOSMCAC, by contrast, uses the ESO to estimate the force error derivative and reconstruct a smooth sliding surface, thereby suppressing noise-induced chattering. The quantitative results for the disturbance and variable stiffness cases (G)–(I) are presented in Table V. Both the 5% settling time and the steady-state MAE are reported for each phase, enabling a comprehensive evaluation of convergence speed and tracking accuracy. These results further demonstrate the robustness and material-independent force-tracking capability of the proposed ESOSMCAC strategy.

In the disturbance rejection cases (G and H), an external force of 5 N is abruptly applied and later removed. Across all three phases in both cases, ESOSMCAC consistently achieves the shortest settling time (0.53–0.82 s) and the lowest MAE (0.0687–0.0958 N). In Case H, the disturbance causes the MAE of AC to more than triple, indicating its high sensitivity to external disturbances when the contact stiffness is large. SMCAC partially mitigates this sensitivity, but its MAE still increases from 0.1707 N to 0.1893 N. In contrast, the MAE of ESOSMCAC remains tightly bounded between 0.0687 N and

Downloaded from https://www.cambridge.org/core. UNIVERSIDAD AUTONOMA METROPOLITANA, on 19 Nov 2026 at 03:47:06, subject to the Cambridge Core terms of use, available at https://www.cambridge.org/core/terms. https://doi.org/10.1017/S0263574726104019

Table V. *Quantitative performance comparison of the three controllers across cases (G)–(I).*

Case	Phase division	Controller Controller	5% Settling time (s)	Steady-state mean absolute error (N)
G	Pre-disturbance	AC	2.120	0.1723
	($t = 0$–8 s)	SMCAC	2.220	0.1609
		ESOSMCAC	1.065	0.0742
	Disturbance applied	AC	1.965	0.1487
	($t = 8$–11 s)	SMCAC	1.030	0.1244
		ESOSMCAC	0.530	0.0958
	Disturbance removed	AC	1.980	0.1191
	($t = 11$–15 s)	SMCAC	1.010	0.1186
		ESOSMCAC	0.815	0.0717
H	Pre-disturbance	AC	2.745	0.1145
	($t = 0$–8 s)	SMCAC	0.925	0.1707
		ESOSMCAC	0.820	0.0706
	Disturbance applied	AC	1.215	0.3464
	($t = 8$–11 s)	SMCAC	0.790	0.1893
		ESOSMCAC	0.540	0.0845
	Disturbance removed	AC	1.180	0.2443
	($t = 11$–15 s)	SMCAC	0.785	0.1575
		ESOSMCAC	0.645	0.0687
I	$K_e = 3$ N/mm	AC	2.120	0.2264
	($t = 0$–7 s)	SMCAC	1.220	0.1754
		ESOSMCAC	1.065	0.0848
	$K_e = 6$ N/mm	AC	2.475	0.1978
	($t = 7$–11 s)	SMCAC	0.790	0.2170
		ESOSMCAC	0.645	0.0865
	$K_e = 2$ N/mm	AC	3.120	0.2870
	($t = 11$–15 s)	SMCAC	1.465	0.1711
		ESOSMCAC	1.170	0.0702

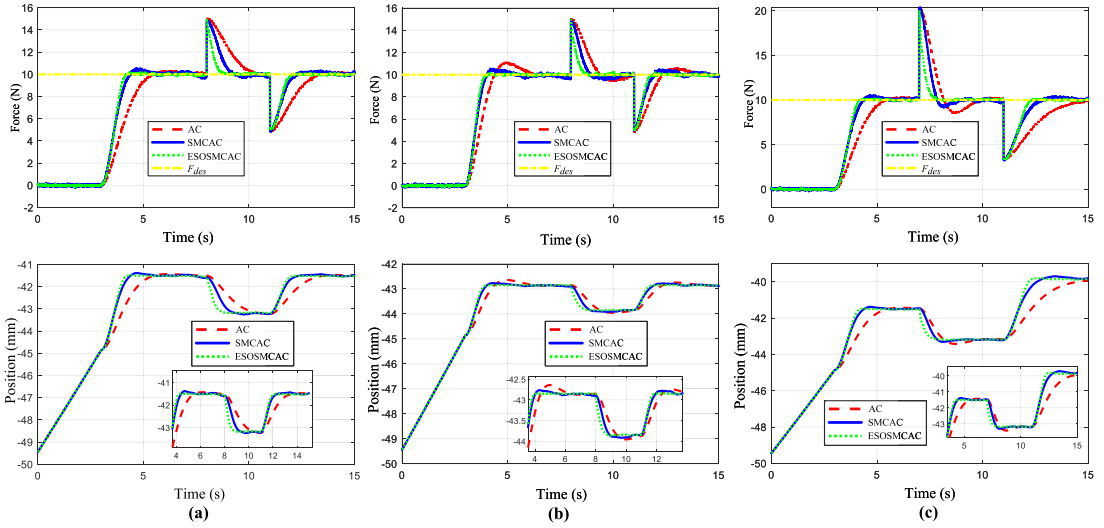


Figure 7. *Force control simulation results for disturbance rejection and time-varying stiffness cases. Subfigures (a)–(b) correspond to Cases G and H. Subfigure (c) corresponds to Case I.*

Downloaded from https://www.cambridge.org/core. UNIVERSIDAD AUTONOMA METROPOLITANA, on 19 Nov 2026 at 03:47:06, subject to the Cambridge Core terms of use , available at https://www.cambridge.org/core/terms. https://doi.org/10.1017/S0263574726104019

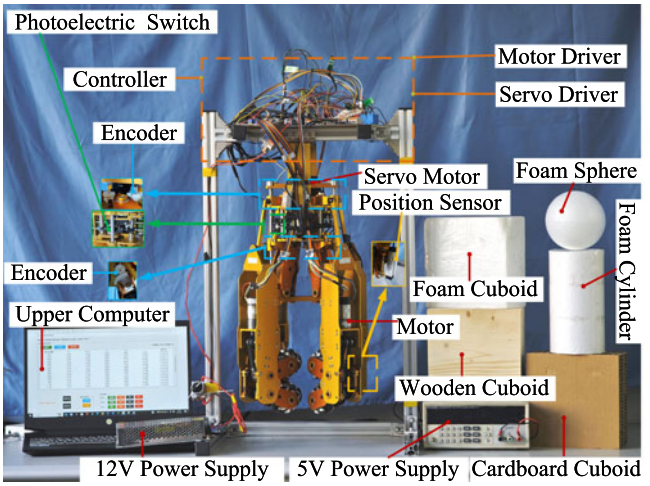


Figure 8. *Experimental platform of the ODH.*

0.0845 N throughout all three phases, demonstrating that the SMC term embedded in the admittance model effectively rejects external disturbances regardless of the environmental stiffness.

In the variable stiffness case (I), the MAE of AC fluctuates considerably with the stiffness change, ranging from 0.2264 N to 0.2870 N. SMCAC exhibits a reduced but still noticeable variation from 0.1711 N to 0.2170 N. By contrast, ESOSMCAC maintains both a consistently short settling time (1.065 s, 0.645 s, and 1.17 s) and a nearly constant MAE (0.0848 N, 0.0865 N, and 0.0702 N) across all three segments. The total variation in MAE is less than 0.017 N over a threefold stiffness range. This near-invariance of both convergence speed and steady-state accuracy under substantial stiffness variation confirms that ESOSMCAC effectively compensates for stiffness-induced uncertainties, achieving material-independent force tracking without requiring stiffness identification.

4.2. Experiments

To evaluate the performance of the ESOSMCAC method during grasping with the ODH, experiments were conducted on a foam sphere, foam cylinders, foam cuboids, cardboard cuboids, and wooden cuboids, using desired contact forces. A comprehensive dexterous-hand experimental platform was constructed, as shown in Figure 8, which includes the ODH body, power supply, host computer, controller, drivers, encoders, servo motors, and displacement sensors.

The grasping process with the ODH can be divided into three phases: ① Free-motion phase: the hand approaches the object gradually; ② Initial-contact phase: the fingertips just make contact with the object; ③ Interaction phase: the hand engages with the object and enters the admittance-control stage.

It should be noted that during the initial contact stage between the ODH and the object, the small angle between the two wheel-fingers of the same finger leads to a prolonged response time for adapting to the object contour. To address this issue, the Mecanum wheels are actively driven to reduce friction between the object and the wheel-fingers, thereby assisting the grasping process. Schematic diagrams of the ODH grasping a foam sphere, a horizontally placed foam cylinder, a vertically placed foam cylinder, a foam cuboid, a cardboard cuboid, and a wooden cuboid are presented in Figure 9. The corresponding grasping results of the three methods are shown in Figure 10. In both grasping and posture-adjustment experiments, the admittance parameters were set as $m=1$, $d=3$, and the ESOSMCAC parameters were chosen as $\lambda=5$, $\rho=5$, $\phi=1$, and $\omega_o=5$. The desired grasping force was set to 10 N for all experiments.

In the hardware experiments, the observer bandwidth was reduced from $\omega_o = 50$ to $\omega_o = 5$ to account for the more complex noise environment of the physical platform. In simulation, a high bandwidth

Downloaded from https://www.cambridge.org/core. UNIVERSIDAD AUTONOMA METROPOLITANA, on 19 Nov 2026 at 03:47:06, subject to the Cambridge Core terms of use, available at https://www.cambridge.org/core/terms. https://doi.org/10.1017/S0263574726104019

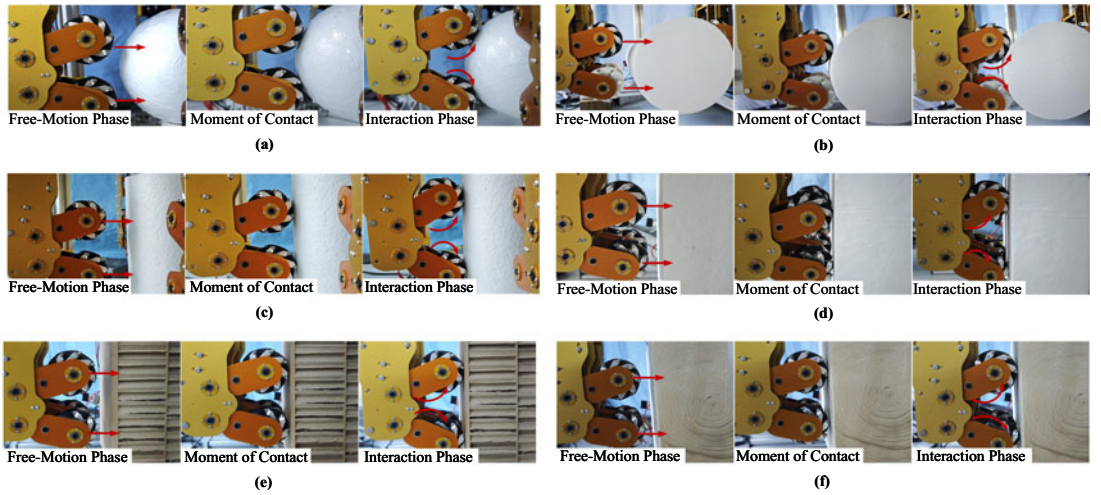


Figure 9. *Grasping processes for (a) a foam sphere, (b) a horizontally placed foam cylinder, (c) a vertically placed foam cylinder, (d) a foam cuboid, (e) a cardboard cuboid, and (f) a wooden cuboid.*

enables fast estimation of the force error derivative under idealized noise conditions. In the physical platform, however, the measured force signal is affected by mechanical vibration, intermittent contact switching of the Mecanum wheel rollers, and other hardware factors, which together introduce more high-frequency components than the idealized simulation noise model. A high observer bandwidth would amplify these components and induce chattering in the reconstructed sliding surface. Therefore, a lower bandwidth was adopted to provide stronger noise attenuation and ensure a smooth sliding surface. This reduction trades slower estimation dynamics for effective suppression of measurement noise, which helps maintain stable force control in the presence of hardware noise.

As shown in Figure 10, after the dexterous hand makes contact with the object and enters the AC phase, the initial response is relatively slow. Once the angle between the wheel fingers reaches a certain threshold, the response rapidly increases, and the actual contact force approaches the desired value, eventually reaching a steady state. Consequently, the position of the dexterous hand ceases to change or varies only slowly. To quantitatively compare the three controllers and assess repeatability, each grasping task was repeated five times for every object. The 5% settling time and the steady-state MAE are reported as mean $\pm$ SD in Table VI.

Across all six objects, ESOSMCAC achieves the shortest or near-shortest settling time and the lowest or near-lowest MAE. The advantage is most pronounced for the horizontal foam cylinder, where ESOSMCAC settles in 6.70 $\pm$ 1.65 s, compared with 24.10 $\pm$ 10.49 s for AC and 20.46 $\pm$ 6.41 s for SMCAC. For the foam sphere, the MAE of ESOSMCAC is 0.1718 $\pm$ 0.0287 N, with an SD substantially smaller than those of AC (0.2878 $\pm$ 0.1170 n) and SMCAC (0.2439 $\pm$ 0.1205 N), indicating superior repeatability. For the wooden cuboid, the three methods yield closer MAE values (ESOSMCAC: 0.2311 $\pm$ 0.0640 N; SMCAC: 0.2265 $\pm$ 0.0529 N; AC: 0.2725 $\pm$ 0.0880 N), as the higher stiffness of wood produces a more stable contact force with smaller inherent fluctuations. Nevertheless, ESOSMCAC consistently outperforms AC and achieves better performance than SMCAC across all tested objects. Grasping performance also varies with object geometry. For spheres and horizontally placed cylinders, the dexterous hand fully envelops the object, achieving complete force closure and thus more stable contact. For cuboids, the fingers adopt an opposing configuration rather than a fully wrapping one; meanwhile, the contact between the Mecanum wheel rollers and the flat surfaces undergoes intermittent switching, resulting in larger force fluctuations. These geometry-dependent differences are further compounded by rigid-body collisions in the mechanical structure and elastic hysteresis in the transmission, which introduce additional force ripples during the dynamic grasping process. Despite

Downloaded from https://www.cambridge.org/core. UNIVERSIDAD AUTONOMA METROPOLITANA, on 19 Nov 2026 at 03:47:06, subject to the Cambridge Core terms of use, available at https://www.cambridge.org/core/terms. https://doi.org/10.1017/S0263574726104019

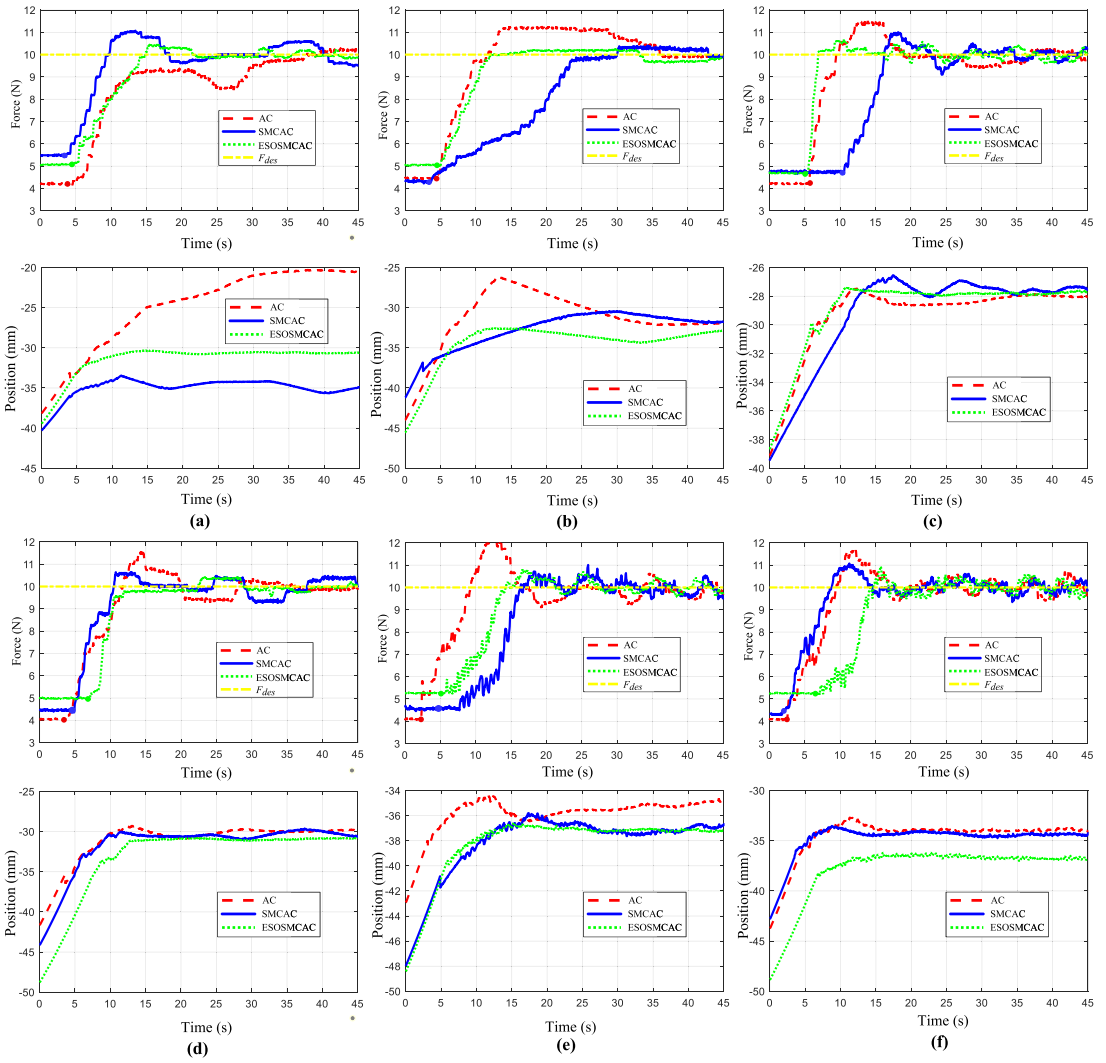


Figure 10. *Force tracking and position responses of the three controllers during grasping of (a) a foam sphere, (b) a horizontally placed foam cylinder, (c) a vertically placed foam cylinder, (d) a foam cuboid, (e) a cardboard cuboid, and (f) a wooden cuboid.*

these mechanical effects, ESOSMCAC maintains robust force tracking across all tested shapes and materials.

In addition, the notable difference in settling time between simulation and hardware experiments can be partly attributed to several physical effects that are absent in the idealized simulation. First, upon initial contact, the small angle between the two whirling fingers of each finger mechanism requires time to adapt to the object contour before stable force closure is achieved; this wheel reconfiguration alignment delays the onset of the AC phase. Second, backlash and elastic hysteresis in the transmission chain, including hinged linkages and gear transmission, slow the closed-loop position response. Third, the communication latency between the controller and the motor drivers introduces a transport delay in the control loop. Nevertheless, the relative performance ranking among the three controllers remains consistent with the simulation results, confirming the robustness of the proposed method under realistic hardware conditions.

Downloaded from https://www.cambridge.org/core. UNIVERSIDAD AUTONOMA METROPOLITANA, on 19 Nov 2026 at 03:47:06, subject to the Cambridge Core terms of use , available at https://www.cambridge.org/core/terms. https://doi.org/10.1017/S0263574726104019

Table VI. *Quantitative comparison of AC, SMCAC, and ESOSMCAC in grasping experiments.*

Case	Controller	5% settling time (s) (Mean ± SD)	Steady-state mean absolute Error (N) (Mean ± SD)
Foam sphere	AC	18.17 ± 9.07	0.2878 ± 0.1170
	SMCAC	15.36 ± 7.74	0.2439 ± 0.1205
	ESOSMCAC	13.77 ± 3.68	0.1718 ± 0.0287
Horizontal foam cylinder	AC	24.10 ± 10.49	0.1669 ± 0.0796
	SMCAC	20.46 ± 6.41	0.2700 ± 0.1377
	ESOSMCAC	6.70 ± 1.65	0.1906 ± 0.0687
Vertical foam cylinder	AC	13.64 ± 8.40	0.3360 ± 0.1048
	SMCAC	8.62 ± 6.09	0.3622 ± 0.0625
	ESOSMCAC	8.27 ± 7.97	0.2132 ± 0.0655
Foam cuboid	AC	17.69 ± 7.97	0.2792 ± 0.0877
	SMCAC	18.18 ± 8.65	0.2654 ± 0.1008
	ESOSMCAC	12.54 ± 8.85	0.2345 ± 0.0566
Cardboard cuboid	AC	15.45 ± 4.24	0.3371 ± 0.0944
	SMCAC	10.74 ± 2.86	0.2945 ± 0.0754
	ESOSMCAC	11.20 ± 3.89	0.2745 ± 0.0794
Wooden cuboid	AC	15.48 ± 5.14	0.2725 ± 0.0880
	SMCAC	13.17 ± 3.10	0.2265 ± 0.0529
	ESOSMCAC	12.08 ± 3.22	0.2311 ± 0.0640

To further validate the ability of the ESOSMCAC method to maintain the desired force during in-hand posture adjustment with the ODH, the omnidirectional mobility of the Mecanum wheels is utilized. A central coordinate system is established for each object. Through the coordinated motion of the Mecanum wheel arrays on the four finger mechanisms, the following adjustments are achieved: rotation of the foam sphere about the z-axis; rotation of the horizontally placed foam cylinder about the x-axis; translation of the vertically placed foam cylinder along the y-axis; and rotation of the cardboard cuboid about the z-axis.

The corresponding Mecanum wheel motion directions for assisted grasping and the above posture adjustments are illustrated in Figure 11(e). The desired force is set to 10 N, and all control parameters remain the same as those used in the grasping phase. The posture-adjustment processes for the respective objects are shown in Figure 11(a)–(d), and the associated force-control and position-tracking performances are presented in Figure 12.

Before adjusting the object posture, the Mecanum wheel-assisted-grasping mode is turned off, and the wheels are then driven according to the required motion directions for posture adjustment. As can be observed from Figure 12, under the action of ESOSMCAC, the grasping force during the posture-adjustment phase remains around 10 N. The steady-state force error across different posture-adjustment tasks ranges from 0.151 N to 0.2598 N. Among these, the sphere and the horizontally placed cylinder exhibit smaller steady-state force errors compared with the other objects. Overall, both the grasping and posture-adjustment experiments further confirm the correctness and effectiveness of the proposed method. The experimental results align well with the earlier theoretical analysis and simulation studies.

5. Conclusion

To address the challenge of force control in grasping and in-hand posture adjustment with the ODH in environments with unknown material properties, this paper first establishes the kinematic model of the ODH using the modified D-H method and a geometric approach, constructs its workspace by sweeping

Downloaded from https://www.cambridge.org/core. UNIVERSIDAD AUTONOMA METROPOLITANA, on 19 Nov 2026 at 03:47:06, subject to the Cambridge Core terms of use, available at https://www.cambridge.org/core/terms. https://doi.org/10.1017/S0263574726104019

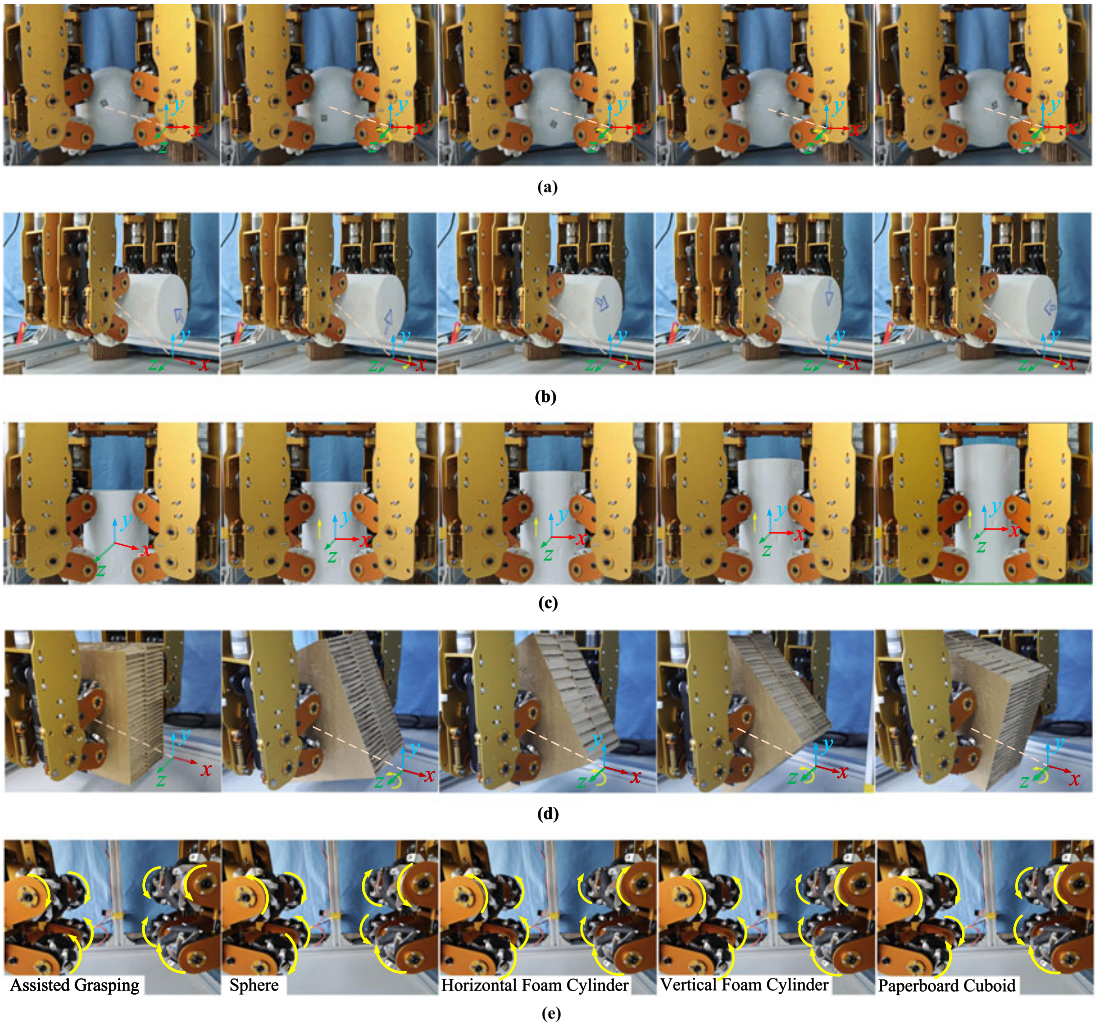


Figure 11. *Posture-adjustment processes for (a) a foam sphere, (b) a horizontally placed cylinder, (c) a vertically placed cylinder, and (d) a cardboard cuboid. (e) Directions of Mecanum wheel motion during assisted grasping and posture adjustment for each object.*

through joint angles, and analyzes the parameter ranges of objects suitable for grasping and posture adjustment. On this basis, a novel AC strategy integrating an ESO with SMC is proposed. Within the virtual mass-damper admittance framework, a sliding-mode term is introduced to enhance robustness against uncertainties in environmental parameters. The ESO estimates and compensates for the noise in the derivative of the force error, reconstructs a smooth sliding surface, and thereby suppresses chattering. A continuous sliding-mode control law, designed via Lyapunov stability theory, ensures stable convergence and smooth force tracking, thereby optimizing the dynamic performance of the AC. Simulation and experimental results demonstrate that the proposed strategy achieves stable convergence and accurate tracking of contact forces under various conditions. This work provides a more robust technical foundation for compliant manipulation with dexterous hands and end effectors. Furthermore, the control framework can be extended to traditional robotic arms and rehabilitation robots, offering an effective solution for adaptive control in tasks such as polishing and grinding, human–robot collaboration, and personalized rehabilitation.

Downloaded from https://www.cambridge.org/core. UNIVERSIDAD AUTONOMA METROPOLITANA, on 19 Nov 2026 at 03:47:06, subject to the Cambridge Core terms of use, available at https://www.cambridge.org/core/terms. https://doi.org/10.1017/S0263574726104019

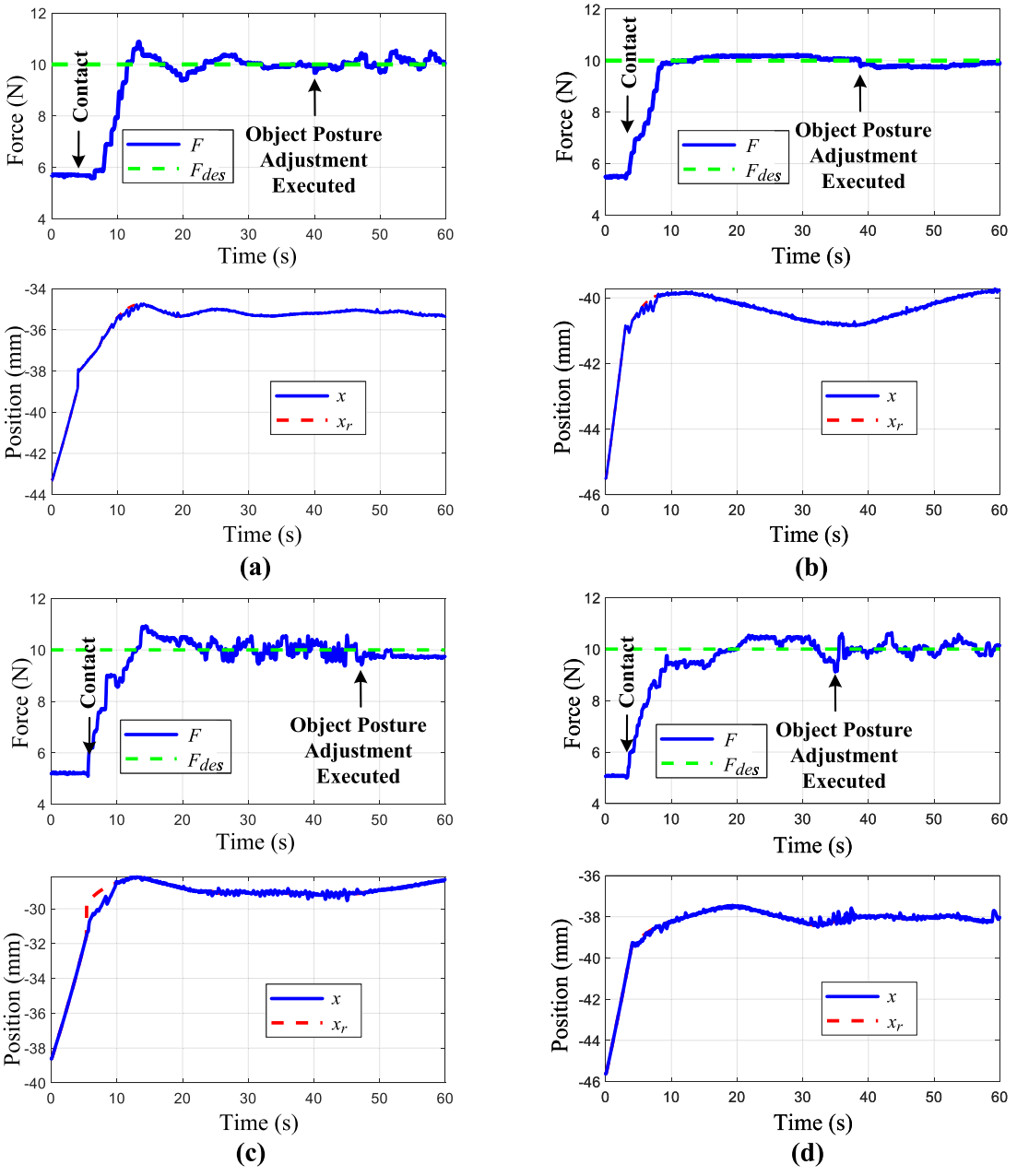


Figure 12. *Force tracking and position responses during posture adjustment of (a) a foam sphere, (b) a horizontally placed cylinder, (c) a vertically placed cylinder, and (d) a cardboard cuboid.*

Author contribution. CY and SL performed conceptualization, methodology, mathematical model derivation, software, and manuscript drafting; SY and HL conducted technical support, manuscript review, and revision.

Financial support. This work was supported by the Basic Scientific Research Operating Funds for Universities in Liaoning Province (Grant numbers LJ222410143019, LJ232410143015).

Competing interest. The authors declare that no conflicts of interest exist.

Downloaded from https://www.cambridge.org/core. UNIVERSIDAD AUTONOMA METROPOLITANA, on 19 Nov 2026 at 03:47:06, subject to the Cambridge Core terms of use, available at https://www.cambridge.org/core/terms. https://doi.org/10.1017/S0263574726104019

Ethical approval. Not applicable.

References

[1] B. Suthar, Y. Abdulrahman and Y. Zweiri, "Robotic fingers: Advancements, challenges, and future directions–a comprehensive review," *IEEE Access* **12**, 110113–110130 (2024).

[2] D. Somma, D. Bianchi, F. Iori, C. Laschi and E. Falotico, "Hand-guided human–robot interaction with a learning-based controller for soft robot arms," *IEEE Access* **14**, 45475–45486 (2026).

[3] O. Faris, H. Alyammahi, B. Suthar, R. Muthusamy, U. H. Shah, I. Hussain and Y. Zweiri, "Design and experimental evaluation of a sensorized parallel gripper with optical mirroring mechanism," *Mechatronics* **90**, 102955 (2023).

[4] X. Chen, K. Zhu, F. He, W. Gao and J. Yao, "A wearable wrist rehabilitation device with vacuum-actuated artificial muscles," *Actuators* **14**, 304 (2025).

[5] C. K. Jha, Y. Shukla, R. Mukherjee, P. Rathva, M. Joshi and D. Jain, "A glove-based virtual hand rehabilitation system for patients with post-traumatic hand injuries," *IEEE Trans. Biomed. Eng.* **71**, 2033–2041 (2024).

[6] F. Zahid, G. E. M. Abro and Z. Alansari, "Recent Advancements in Manipulator-Equipped Unmanned Aerial Vehicles (UAVs)," **In:** *2024 1st Int. Conf. on Innovative Engineering Sciences and Technological Research (ICIESTR)*, (2024) pp. 1–4.

[7] H. Wang, H. Xu, F. J. Abu-Dakka, V. Kyrki, C. Yang, X. Li and S. Chen, "A bidirectional soft biomimetic hand driven by water hydraulic for dexterous underwater grasping," *IEEE Robot. Autom. Lett.* **7**, 2186–2193 (2022).

[8] H. Chen, W. Xu, W. Guo and X. Sheng, "Variable admittance control using velocity-curvature patterns to enhance physical human–robot interaction," *IEEE Robot. Autom. Lett.* **9**, 5054–5061 (2024).

[9] Y. Pi, S. Feng, Q. Chen and K. Wu, "Adaptive Admittance Control for Active Compliance Under Dynamic Motion," **In:** *2024 10th Int. Conf. on Electrical Engineering, Control and Robotics (EECR)*, (2024) pp. 140–145.

[10] C. Liu and Z. Li, "Force tracking smooth adaptive admittance control in unknown environment," *Robotica* **41**, 1991–2011 (2023).

[11] C. Gao, C. Wang, H. Li, J. Zhang, X. Du and J. Zhang, "Human–machine coupling dynamics modeling and adaptive admittance control of lower limb rehabilitation robot," *Robotica* **43**, 1–23 (2025).

[12] D. X. Ye, C. G. Yang, Y. M. Jiang and H. Zhang, "Hybrid impedance and admittance control for optimal robot-environment interaction," *Robotica* **42**, 510–535 (2024).

[13] K. Li, X. Xiong, A. Wang, Y. Qu and Y. Lou, "Implicit Euler discrete-time set-valued admittance control for impact–contact force control," *IEEE/ASME Trans. Mechatron.* **29**, 1–11 (2024).

[14] S. Jung, "Admittance Force Tracking Control for Position-Controlled Robot Manipulators Under Unknown Environment," **In:** *2020 20th Int. Conf. on Control, Automation and Systems (ICCAS)*, (2020) pp. 219–224.

[15] Q. Shi, S. He, H. Wang, V. Stojanovic, K. Shi and W. Lv, "Extended state observer based fractional order sliding mode control for steer-by-wire systems," *IET Control Theory Appl.* **18**, 2287–2295 (2023).

[16] H. V. Dao and K. K. Ahn, "Extended sliding mode observer-based admittance control for hydraulic robots," *IEEE Robot. Autom. Lett.* **7**, 3992–3999 (2022).

[17] N. V. Toan and P. B. Khoi, "Fuzzy-based-admittance controller for safe natural human–robot interaction," *Adv. Robot.* **33**, 815–823 (2019).

[18] Y. Liu, J. Huang, Y. Jia, L. Zhou and G. Li, "Robotic Precision Force Control in Optical Machining a Fuzzy Admittance Approach," **In:** *2023 5th Int. Conf. on Robotics, Intelligent Control and Artificial Intelligence (RICAI)*, (2023) pp. 210–214.

[19] K. Almaghout, B. Tarvirdizadeh, K. Alipour and A. Hadi, "RBF neural network-based admittance PD control for knee rehabilitation robot," *Robotica* **40**, 4512–4534 (2022).

[20] Z. Wang, J. Lei and G. Zheng, "Neural network adaptive admittance control for improving position/force tracking accuracy of fracture reduction robot," *Trans. Inst. Meas. Control.* **47**, 1–12 (2025).

[21] L. X. Wang, C. Y. Chen, C. C. Wang, K. C. Ying, Y. B. Li and G. L. Yang, "A stability observer for human–robot and environment-robot interaction with variable admittance control," *Int. J. Adv. Manuf. Technol.* **128**, 437–450 (2023).

[22] L. Chen, Z. Jin, K. Shao, G. Wang, S. He, V. Stojanovic and H. Wang, "Adaptive integral terminal sliding mode control of unmanned bicycle via ELM and barrier function," *Robotica* **42**, 2635–2657 (2024).

[23] M. Zhu, C. Huang, S. Song, Y. Zhao, J. Qi and D. Gong, "Adaptive vision-admittance-based leakage-type sliding mode control for uncertain collaborative robot with actuator saturation," *IEEE Trans. Syst. Man Cybern. Syst.* **55**, 8412–8423 (2025).

[24] H. Gao, C. Ma, X. Zhang and C. Zhou, "Compliant variable admittance adaptive fixed-time sliding mode control for trajectory tracking of robotic manipulators," *Robotica* **42**, 1731–1760 (2024).

[25] W. Khalil and J. F. Kleinfinger, "Minimum operations and minimum parameters of the dynamic models of tree structure robots," *IEEE J. Robot. Autom.* **3**, 517–526 (1987).

[26] J. Duan, Y. Gan, M. Chen and X. Dai, "Adaptive variable impedance control for dynamic contact force tracking in uncertain environment," *Robot. Auton. Syst.* **102**, 54–65 (2018).

[27] D. Xu, L. Yin and J. Wang, "Grinding force estimation and control of grinding robot with variable impedance control strategy," *Int. J. Adv. Manuf. Technol.* **137**, 2011–2027 (2025).

Cite this article: C. Ye, S. Lu, S. Yu and H. Li, "Extended state observer-sliding mode admittance control for grasping by the omnidirectional dexterous hand", Robotica. https://doi.org/10.1017/S0263574726104019

Downloaded from https://www.cambridge.org/core. UNIVERSIDAD AUTONOMA METROPOLITANA, on 19 Nov 2026 at 03:47:06, subject to the Cambridge Core terms of use, available at https://www.cambridge.org/core/terms. https://doi.org/10.1017/S0263574726104019